Heterogeneous water distribution in between peridotite xenoliths from Kaapvaal Craton kimberlites: Constraints on diamond barren nature of kimberlites

Sahroz Khan [a,*], Nóra Liptai [b,c], István J. Kovács [b,c], Yana Fedortchouk [d], Tivadar M. Tóth [a]

[a] Department of Mineralogy, Geochemistry and Petrology, University of Szeged, Hungary
[b] MTA FI Lendület Pannon LitH2Oscope Research Group, Institute of Earth Physics and Space Science, Sopron, Hungary
[c] Institute of Earth Physics and Space Science, Eötvös Loránd Research Network, Sopron, Hungary
[d] Department of Earth and Environmental Sciences, Dalhousie University, Halifax, Canada

ABSTRACT

Nominally anhydrous mantle minerals (olivine, pyroxenes, garnets, etc.) in 11 peridotite xenoliths from four different uneconomic and economic Kaapvaal Craton kimberlite pipes (Matsoku, Thaba Putsoa, Pipe 200 and Bultfontein) have been investigated using Fourier transform infrared spectroscopy (FTIR). All xenoliths contain accessories of garnet, diopside, chromite, and phlogopite. High orthopyroxene content (>30 mol vol.%) in most xenoliths from all kimberlites and its interconnected channel-like nature hint towards hydrous siliceous fluid metasomatism. Peridotite xenoliths from uneconomic kimberlites show development of phlogopite and clinopyroxene (± chromite) forming veins and in garnet rims suggesting metasomatism by alkaline silico-carbonatite (possibly kimberlite-related) melt. The xenoliths contain significant H_2O in olivine (17–62 ppm), orthopyroxene (21–230 ppm), and clinopyroxene (87–833 ppm), whereas garnets are dry and only show IR absorbance bands at > 3,670 cm^{-1} for contamination of hydrous minerals. Compared to the economic kimberlites in the Kaapvaal Craton, the uneconomic kimberlite xenoliths from this study have lower orthopyroxene and olivine H_2O content. In the xenoliths affected by garnet breakdown metasomatism, the H_2O content of orthopyroxene and olivine is higher and lower, respectively. The structural hydroxyl distribution profile across olivine and higher inter-mineral water partition coefficient, suggest diffusion of hydrogen and possible re-equilibration. Statistical analysis of the olivine spectra suggests that hydrogen bands at 3540, 3624, 3638, and 3672 cm^{-1} are a good discriminant of economic and uneconomic kimberlites and in literature, they are associated with metasomatism, weathering-associated processes, high water activity, and oxygen fugacity. The lower water concentration in xenoliths from uneconomic kimberlite from the margin of the craton than the economic kimberlites from the interior of the Kaapvaal Craton and identified meta-somatism hints towards dehydration of xenoliths by water-poor and CO_2-rich melts in tectonized cross-lithospheric zones causing diamond resorption and may be responsible for the diamond-poor nature of uneconomic kimberlites in northern Lesotho.

1. Introduction

Kimberlites are volatile-rich ultramafic magmas derived from mantle depths (>150 km) and are economically significant because they are the major host of diamonds. Mantle xenoliths are often transported by kimberlites, providing fundamental information on both the magmas transporting them and the evolutionary history of the subcontinental lithospheric mantle (SCLM). The disintegration of entrained mantle xenoliths liberates high-pressure minerals and diamonds derived from the mantle. Although the quantities of liberated diamonds are minor, sometimes they can be present in economic quantities. The presence of diamonds depends primarily on the mantle source sampled by the kimberlite and owing to the instability of diamonds at lower pressure and high temperature, they must be brought to the surface rapidly by magmas travelling at very high ascent rates of m/s calculated for

some economic kimberlites (Peslier et al., 2008). In the case of slower ascent, diamonds if present may undergo dissolution or graphitization, rendering the kimberlite uneconomic as are most kimberlites worldwide (de Wit et al., 2016).

Diamond dissolution and loss of diamond grade occur during its ascent in the kimberlite magma as well as in the mantle source during melt metasomatism (Fedortchouk et al., 2022, and references therein). Dissolution of lithospheric diamond in the mantle source is linked to melt metasomatism (Fedortchouk et al., 2019), and the composition of the solvent plays a vital role in the morphology and dissolution of diamonds during ascent·H_2O is a fundamental component affecting both the growth and dissolution of diamonds (Palyanov and Sokol, 2009; Khokhryakov and Pal'yanov, Y.N. 2010) and its concentration in the mantle source of diamond may significantly affect the diamond grade. Nominally anhydrous minerals serve as an important host of H_2O in the mantle. They can incorporate several protons (H^+) attached to structural oxygen (O) in intrinsic crystal defects (Bell and Rossman, 1992; Kovács et al., 2010; Miller et al., 1987; Peslier et al., 2010), and this structural hydroxyl is commonly called 'water'. Water content affects melting temperature (e.g., Green et al., 2010; Grove et al., 2006; Katz et al., 2003), electrical conductivity/resistivity (Fullea, 2017), seismic wave attenuation(Aizawa et al., 2007), and deformation behavior (Liptai et al., 2021, and references therein) of SCLM rocks.

Water content of primary kimberlite melt, which is not well constrained, determines its composition in terms of carbonate and silicate as well as the temperature of melting (e.g. Stamm and Schmidt, 2017). The recent studies on back-calculation of kimberlite melt composition and melt inclusions suggest a higher alkali-rich carbonate or carbonate–silicate nature of primary kimberlite melts (Brooker et al., 2011; Kostrovitsky et al., 2023; Giuliani et al., 2020; Golovin et al., 2020, 2007; Sharygin et al., 2022; etc.). The content of both volatiles (H_2O and CO_2) in the kimberlite melt is obscured by significant modification of composition due to entrainment and assimilation from the mantle cargo picked up during ascent, loss of volatiles during explosive eruption, and serpentinization by surface fluids (Moussallam et al., 2015). The CO_2 solubility study in kimberlite melts of Moussallam et al. (2015) suggests CO_2 exsolution and degassing take place at shallower depths. In the melt inclusion studies by Abersteiner et al. (2022), they demonstrate that during exsolution, CO_2 is well partitioned in the vapor phase, and H_2O is retained longer in the melt during degassing and later lost through diffusion. Similarly, in the kimberlite melt, olivine loses water to the kimberlite magma (Hilchie et al., 2014), and the fluid component of kimberlite melt takes part in the oxidation reaction leading to the dissolution of diamonds (Fedortchouk et al., 2007).

Minerals inside mantle xenoliths entrained by the kimberlite magma are largely shielded from the alteration by the kimberlitic melt because kimberlite magma comes from great depths at very fast ascent rates and provide an opportunity to study the mantle processes. Storage of water in olivine, orthopyroxene, clinopyroxene, and garnets from xenoliths and megacrysts from the Kaapvaal Craton has been extensively studied (Baptiste et al., 2012; Bell et al., 2004; Bell and Rossman, 1992; Bonadiman et al., 2009; Demouchy and Bolfan-Casanova, 2016; Grant et al., 2007; Ingrin and Grégoire, 2010; Jackson and Gibson, 2023; Kent and Rossman, 2002; Kurosawa et al., 1997; Peslier et al., 2012, 2010, 2008; Schmädicke et al., 2015). The reported water concentration shows a significant variation between kimberlites and localities within the Kaapvaal Craton, reflecting the heterogeneity in H_2O content in space and time across the craton. Grant et al. (2007) studied the water partitioning between the different nominally anhydrous minerals and found differences in the partitioning between clinopyroxene and olivine, which is controlled by their structure or composition or both. Peslier et al. (2008) detected lower H contents at the edges of olivine grains and used diffusion modelling of H profiles to calculate extremely high kimberlite ascent rates of 5–37 ms^{-1} (Peslier and Luhr, 2006). Temporal variation was recorded in xenoliths from older Group II kimberlites (now reclassified as carbonate-rich olivine lamproites-CROL) showing low water concentration than in younger Group I kimberlites of ∼ 90 Ma from South Africa showing higher water concentration (Ingrin and Grégoire (2010). Water concentration in xenoliths from the closely spaced (15 km apart) Letseng and Liqhobong kimberlites was used to examine variation in their metasomatic history (Peslier et al., 2012). Due to metasomatism by water-poor melts of fluids, xenoliths from Letseng kimberlites have a very low water concentration as compared to the higher water concentration in xenoliths from Liqhobong kimberlite metasomatized by hydrous, alkaline, siliceous fluids or melts. The vertical variation in the distribution of water in the continental lithospheric mantle of Kaapvaal Craton has been well-established in several articles (Baptiste et al., 2012; Doucet et al., 2014; Peslier et al., 2010). They found water-poor olivine at the deeper lithosphere-asthenosphere boundary and higher water concentration in olivine from the shallower mantle. The dry metasomatism of olivine at greater depths and migration of water into peridotites at shallower depths is explained as the likely cause (Doucet et al., 2014). While pyroxenes control the bulk water concentration of peridotites and the mantle, the higher modal proportions of olivine in peridotites control the physical properties of the lithospheric mantle (Demouchy and Bolfan-Casanova, 2016). The most recent study of xenoliths from Bultfontein and Mothae kimberlites by Jackson and Gibson (2023) found a correlation between the style of metasomatism and water and F content. The subduction-derived silicic fluids mainly cause the enrichment in water, whereas the proto-kimberlite melts cause the enrichment in both water and F. The similarity in the highest water concentration of sheared peridotites entrained from the base of the central Siberia craton by Udachnaya kimberlites and highly-metasomatized and sheared high-temperature garnet peridotites are entrained from the base of the southeast margin of Kaapvaal craton by Mothae kimberlite is also extended to suggest a correlation between water contents and deformation. Compared to the mechanical boundary layer model of Peslier et al. (2010), Jackson and Gibson (2023) suggest that the dehydrated olivine from high-temperature garnet peridotites forms a thermal layer which is a result of a large amount of adiabatic melting. The higher water content is due to addition of volatiles over a short span of 20 Ma between the eruption of the two Cretaceous kimberlite emplacement pulses.

All these previous studies of H distribution and water concentration heterogeneity in nominally anhydrous minerals from Kaapvaal Craton peridotites used to understand the mantle metasomatic (dry or wet) depletion or enrichment events, kimberlite ascent rates, diamond formation and destruction, geodynamics, and other processes have been focused on economic kimberlites. Therefore, they may give a biased picture of kimberlite evolution and its role in diamond preservation. Here we present the results of FTIR analysis of xenoliths from both the economic and uneconomic kimberlites in order to understand the processes that affect diamond preservation/destruction in the mantle and during the kimberlite ascent. We concentrate on xenoliths from uneconomic (Matsoku, Thaba Putsoa and Pipe 200) and economic (Bultfontein) kimberlites, focusing on their H distribution and water contents in conjunction with the textural features and comparing them with other kimberlites from the literature. We also study the metasomatic history of these xenoliths and use statistical analysis of the olivine FTIR spectra to develop a method for differentiating between economic and uneconomic kimberlite types.

2. Geological background

The Kaapvaal Craton covers an area of 1.2 million km², and it formed and stabilized between 3.7 and 2.6 Ga (de Wit et al., 1992; Griffin et al., 2003). It consists of two major Archean terranes − the Witwatersrand block (3.55 to 3.08 Ga) in the east is joined to the Kimberley block (3.15 to 2.09 Ga) in the west. The collision of the two blocks at 2.9 Ga along the Colesberg lineament (Fig. 1) led to the co-eval subduction of eclogitic material in the mantle (Bell et al., 2005; Richardson et al., 2001; Schmitz et al., 2004; Wasch et al., 2009). The craton is represented by an assemblage of early Archean granite-greenstone terranes and older tonalitic gneisses, which have been intruded by granitic plutons (3.3 to 3.0 Ga). The rocks are overlain by a thick succession of sedimentary and volcanic rocks in the late Archean basins. It is affected by multiple collision events along the margins. It is bordered on the west by Khesi orogenic belt (2.0–1.7 Ga) and on the south by the Namaqua belt (1.2–2.0 Ga) (Fig. 1) of Proterozoic origin formed during collisional events (Jacobs et al., 2008). The eastern boundary is flanked by the Lebomo monocline (2.0–1.7 Ga) and late archean Limpopo belt (2.8–2.5 Ga) (Fig. 1) on the north welds Kaapvaal Craton to the Zimbabwe craton.

The craton has been affected by many post-Archean magmatic events. The most significant is the emplacement of the Bushveld complex of 2.06 Ga age (Fig. 1) (Scoates and Friedman, 2008). Kaaroo large igneous province extrusion is of 182 Ma age and is associated with the Gondwana breakup (Riley et al., 2006). The Kaapvaal Craton is punctuated by kimberlites after 1.8 Ga with peak kimberlite magmatic activity at 90 ± 10 Ma which was significant even at 60 ± 10 Ma (Tappe et al., 2018). The micaceous Group II kimberlites (reclassified as carbonate-rich olivine lamproites-CROL by Pearson et al., (2019)) are > 110 Ma in age, whereas Group I or archetypal kimberlites are of ≤ 100 Ma age(Kobussen et al., 2009). The mantle sampled by CROL is thick, cooler, depleted, and less metasomatized as compared to the Group I kimberlites, which intruded a relatively thinner and fertilized SCLM with a raised geotherm and did not represent primary SCLM compositions (Griffin and O'Reilly, 2007; Kobussen et al., 2008; O'Reilly and Griffin, 2010).

Three metasomatic events are recorded in the helium isotope ratios of high-density fluid in diamonds (Weiss et al. (2021) from De Beers Pool and Finsch mines: highly saline fluids during the Cretaceous, silicic fluids during the Paleozoic, and carbonatitic fluids during the Proterozoic. In the study of Ti, Zr, Y contents of peridotitic garnet xenocrysts from the Kaapvaal Craton Group I kimberlites and CROL along an SW to NE traverse, the SW domain is metasomatized by mafic silicate melts, the central domain is affected by the hydrous, highly alkaline fluid (phlogopite-style metasomatism) and the northeastern domain is affected by high Fe signature of Bushveld complex (Kobussen et al., 2009). The high amounts of orthopyroxene in the lithospheric mantle are associated with volatile silica enrichment due to subsequent metasomatic events during the collision of Kaapvaal blocks, during the Proterozoic (Wasch et al., 2009) and Paleozoic (Weiss et al., 2021). The diamond growth events are reflected in the enrichment/metasomatism by large igneous events like Proterozoic subduction processes at the craton margins; Bushveld complex emplacement; Karoo magmatism; Jurassic-Cretaceous magmatism associated with the lamproite and Cretaceous kimberlite formation (Aulbach et al., 2021; Gregoire et al., 2003; Lazarov et al., 2012; Richardson et al., 1990, and references therein).

2.1. Kaapvaal craton kimberlites

2.1.1. Matsoku kimberlite

The Matsoku kimberlite is a small, elliptical diatreme (90 x 35 m) located in northern Lesotho. It intruded the Karoo supergroup Stormberg lavas at 94.7 Ma (Olive et al., 1997; Tappe et al., 2018). Matsoku kimberlite is a barren kimberlite representing single magmatic phases (Cox et al., 1973). The xenoliths in Mat-
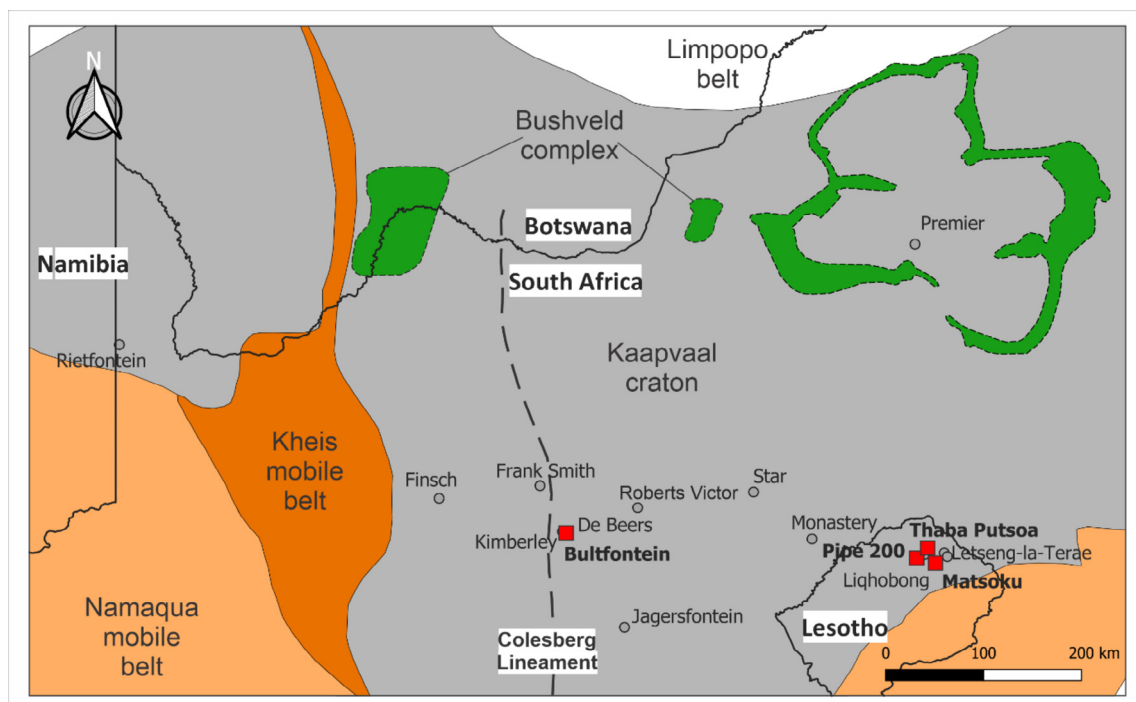
Fig. 1. Geological map showing the Kaapvaal Craton, Proterozoic terranes, and mobile belts in southern Africa modified after Tappe et al. (2021). The location of kimberlites from this study (red squares) in Lesotho and South Africa are compared with some kimberlites from the literature (gray circles). The Colesberg lineament is shown as a dashed line.

soku kimberlite are abundant and fresh (Cox et al., 1973). They have peridotitic and pyroxenitic affinity and have been extensively studied by (Harte, 1983; Harte et al., 1987; Harte et al., 1993) who identified different xenolith types in the order of abundance including: (i) coarse clinopyroxene-poor garnet lherzolites; (ii) coarse unmetasomatised xenoliths enriched in clinopyroxene and garnet; (iii) metasomatized xenoliths showing melt infiltration, and (iv) xenoliths showing contact between coarse xenolith and intrusive metasomatic veins.

2.1.2. Thaba Putsoa kimberlite

The Thaba Putsoa kimberlite is a diamond barren kimberlite with an age of 89 Ma situated in the mountains in northern Lesotho (Tappe et al., 2018). It contains different types of xenoliths including granular spinel lherzolite, granular graphite-bearing garnet-spinel harzburgite, sheared porphyroclastic dunite, etc. (Boyd and Nixon, 1975). Compared to other Kaapvaal Craton kimberlites, dunite xenoliths are much more common and have a porphyroclastic texture similar to that shown by sheared lherzolites (Boullier and Nicolas, 1975). Ni-Mg rich olivine neoblasts in Fe-rich olivine from Thaba Putsoa kimberlite dunites are compared to Ni-bearing sulfides in the most Fe-rich olivine megacrysts from nearby Monastery kimberlite and suggested to form due to the development of sulfide immiscibility, infiltration of Ni-Mg-rich magma in earlier crystallized Fe-rich olivine and dunites (Toth and Schulze, 2017).

2.1.3. Pipe 200 kimberlite

Pipe 200 is located in Northern Lesotho close to the Letele Pass and west of Kao area kimberlites and has a total size of 1.2 ha. The outcrops are on the western bank of the Malibamatso river, where the pipe is characterized by multiple phases of coherent (CK) and volcaniclastic kimberlite (VK) kimberlite (Hilchie, 2011). It has a low diamond grade of 0.02 carats/t (Tappe et al., 2018) and is considered uneconomic because two of the three intrusions do not contain diamonds (Kresten and Dempster, 1973). Like other Group I kimberlites in Northern Lesotho, it is dated at ∼ 90 Ma (Davis, 1977; Tappe et al., 2018). The kimberlite contains crustal xenoliths (sandstone, basalts, etc.) along with lherzolites and harzburgites (Mitchell et al., 1980).

2.1.4. Bultfontein kimberlite

Bultfontein kimberlite is a part of the Kimberley cluster, which includes De Beers, Dutoitspan, Wesselton, Kimberley, and Kamfersdam kimberlite pipes and other smaller pipes and sills. It is located on the western terrane of Kaapvaal Craton and has a size of 9.7 ha (Tappe et al., 2018). Bultfontein kimberlite is composed of three lithologies: diatreme facies tuffistic kimberlite breccia (B1), hypabyssal facies kimberlite breccia (B2) enveloping B1 and NNW extension (enlargement of a dyke) (B3) (Clement, 1982; Field et al., 2008). It is a typical Group I kimberlite of Cretaceous age confirmed by Rb-Sr dating (84 ± 3 Ma) of phlogopites by Allsopp and Barrett (1975) and U-Pb dating (∼81.7 to ∼ 91.2 Ma) of zircons by Davis (1977). It is one of the well-known economic mines in southern Africa, known for its consistent diamond grade of 0.54 carats/t (Tappe et al., 2018) and thus has been extensively studied. The xenoliths from the Bultfontein pipe are detailed out in Lawless et al. (1979) and Field et al. (2008) and consist of lherzolites, harzburgites, mica-rich rocks (MARID suite), rare dunite, wehrlite, and eclogites, etc. Rare polymict breccias which are a mixture of mantle-derived grains set in a relatively fine-grained matrix of olivine, phlogopite, ilmenite and rutile, etc. are present as well (Sharygin et al., 2022).

3. Sampling and analytical methodology

The xenoliths were collected by Dr. Barrie Clarke in 1973 during field trips associated with the 1st International Kimberlite Conference. The sample preparation for FTIR analyses is detailed in Hilchie et al. (2014) and the same samples prepared by Luke Hilchie are used in this study. The thick sections were prepared by polishing both sides of each xenolith nodule. The description of the sample modal mineralogy and thickness is given in Tables 1 and 2, respectively. Eleven of the sixteen thick sections, which contained unaltered, predominantly unfractured, and inclusion-free clear crystals, were chosen for FTIR analyses. After photography, the thick sections were separated from their glass slide by immersion in acetone and dissolution of the glue for FTIR analyses.

3.1. Fourier transform infrared spectroscopy

FTIR spectroscopy was carried out on the eleven xenoliths using unpolarized light to study the hydrogen distribution and calculation of the water contents. Measurement was carried out at the Institute of Geological and Geochemical Research, Budapest, using a Bruker FTIR Vertex 70 spectrometer equipped with a Globar light source. Additional measurements were carried out using an MCT-A detector coupled to a Bruker Hyperion 2000 microscope at the Budapest University of Technology and Economics, using the Perkin Elmer Spectrum 400 infrared spectrometer along with a coupled Spotlight 400 FTIR imaging system. The analysis was carried out on unoriented xenoliths of 255 to 447 μm double polished thickness (Table 1) using a 50×50 μm aperture. The spectral range for olivine and pyroxene is 4000 and 600 cm^{-1} and 4000 and 750 cm^{-1}, respectively. Background and scans were carried out at 128 scans at 4 cm^{-1} resolution. The Integrated absorbance was calculated on five differently oriented olivine grains using OPUS software. Similarly, in each thick section, one to three differently oriented orthopyroxene and one to two differently oriented clinopyroxene grains were used. Unfractured, clear, and fresh olivine and pyroxene grains were used for measurement to avoid serpentine.

The water concentration of orthopyroxene and clinopyroxene are slightly underestimated and overestimated, respectively. This is because of slight overlap of water absorption band in the pyroxene spectra with serpentine absorption band which was cut out from the integration wavenumber range and cutting of spectra to avoid it. In the case of orthopyroxene and clinopyroxene the slight overlap of was excluded and included, respectively causing the slightly underestimation and overestimation of water concentration.

For accurate measurement of water concentration, the spectra were inspected for serpentine absorption bands which, if present, were removed (cut) from the spectra for integration. The water concentration for orthopyroxene and clinopyroxene in some xenoliths may be slightly underestimated and overestimated, respectively and shown in bold in Table 3. This is because of slight overlap of water absorption band in the pyroxene spectra with serpentine absorption band which was cut out from the integration wavenumber range and cutting of spectra to avoid it. In the case of orthopyroxene and clinopyroxene the slight overlap of was excluded and included, respectively and may result in slight underestimation and overestimation of water concentration.Baseline correction was performed using the concave rubberband correction routine with two iterations and 64 baseline points to ensure that the baseline of all spectra is at zero absorbance. Integration was done using B-type integration for uniform intervals of the mineral in which the software automatically draws a baseline for

Table 1
Petrography and modal composition of the studied Kaapvaal Craton xenoliths from four kimberlite pipes from Lesotho and South Africa. The xenoliths with garnet breakdown assemblage of Chr, Phl, and Di are shown in bold. Ol- Olivine; opx- orthopyroxene; cpx- clinopyroxene; gt- garnet; chr- chromite; phl- phlogopite.

Xenolith	Pipe	Assemblage	Modal abundance					
			Ol	Opx	Cpx	Gt	Chr	Phl
8A	Matsoku	Grt + Di	63	31	1	5	–	–
8B	Matsoku	**Grt + Chr + (Chr + Phl + Di)**	51	37	0.2	8	3	<1
9	Matsoku	**Grt + (Chr + Phl + Di)**	25	69	1	5	–	<1
16A	Thaba Putsoa	**Grt + Chr + (Chr + Phl + Di)**	60	37	<1	3	<1	<1
16B	Thaba Putsoa	**Grt + Chr + Di + (Chr + Phl + Di)**	55	42	<1	3	<1	1
29A	Pipe 200	Grt + Di + Chr	61	37	–	1	1	–
29B	Pipe 200	Grt + Di + Chr	63	35	0.3	2	<1	–
32B	Pipe 200	**Grt + Di + Chr + (Chr + Phl + Di)**	80	19	<1	<1	1	<1
32C	Pipe 200	**Grt + Di + Chr + Phl+ (Chr + Phl + Di)**	78	15	2	2	1	3
51	Bultfontein	Grt + Di	61	35	<1	4	<1	–
55A	Bultfontein	Grt + Chr	75	17	–	8	2.0	–

Table 2
Classification of harzburgite xenoliths according to the aluminous phase, orthopyroxene content, and primary and secondary clinopyroxene.

		Opx-rich (> 30 %)		Opx-poor (< 20 %)	
		Secondary cpx	Primary cpx only	Secondary cpx	No cpx
Garnet-Spinel harzburgite	Secondary Chromite	8B 9		32B 32C	
	Primary chromite	16A 16B	29A 29B		55A
Garnet harzburgite	No chromite	8A 51			

Table 3
Calculated integrated absorbance and water content (in ppm wt.) measured in the studied Kaapvaal Craton xenoliths from four kimberlite pipes from Lesotho and South Africa. The water concentration in bold is affected by serpentine bands and may be slightly underestimated and overestimated in orthopyroxene and clinopyroxene, respectively.

Sample	Pipe	Garnet breakdown assemblage	Thickness	Olivine		Orthopyroxene		Clinopyroxene	
				Absorbance	H_2O ppm	Absorbance	H_2O ppm	Absorbance	H_2O ppm
8A	Matsoku	–	447	2.2	27	21	94	9.3	87
8B	Matsoku	+	388	1.7	24	22.0	115	30.6	331
9	Matsoku	+	446	–	–	32.0	145	48.8	460
16A	Thaba Putsoa	+	427	2.3	30	26.3	**125**	–	–
16B	Thaba Putsoa	+	385	1.7	25	43.6	230	–	–
29A	Pipe 200	–	429	2.5	33	19.6	**92**	–	–
29B	Pipe 200	–	377	1.8	27	8.3	**44**	66.1	**737**
32B	Pipe 200	+	256	0.9	20	–	–	–	–
32C	Pipe 200	+	286	0.9	17	3.0	**21**	56.8	833
51	Bultfontein	–	424	3.1	41	36.8	175	61.1	**604**
55A	Bultfontein	–	379	4.1	62	11.3	60	–	–

the entered start and end points where the absorbance is minimum. The calculation of the water content in ppm wt. was made using the method of Sambridge et al. (2008) and Kovács et al. (2008), which is applicable for < 0.15 maximum linear unpolarized absorbance. The water content was quantified using total polarized absorbance (A_{tot}), three times the average unpolarized integrated absorbance and calibration factors. The calibration factor for olivine (k_{ol} = 0.188) was taken from Bell et al. (2003), and for orthopyroxene (k_{opx} = 0.0674) and clinopyroxene (k_{cpx} = 0.14) was taken from (Bell et al., 1995). The water concentration was normalized to 1 cm thickness. Thickness measurements (Table 3) were averaged from 5 to 6 spots on the thick sections using a Mitutoyo analogue micrometer on the thick sections. The integrated absorbance is tabulated in Table 3. The cumulative uncertainty of this method does not exceed 30 % (Kovács et al., 2008; Liptai et al., 2023; Patkó et al., 2019).

3.2. X-ray fluorescence spectroscopy

Elemental mapping using Energy dispersive (EDS) multielement micro X-ray fluorescence (µXRF) was carried out using a Horiba

Jobin Yvon XGT-5000 X-ray fluorescent spectrometer on xenolith thick sections at the department of Mineralogy, Geochemistry and Petrology at the University of Szeged. The spectrometer is equipped with a Rh X-ray source. The measurement conditions were set to 30 kV beam voltage, 0.5 mA beam current, and 10 µm beam spot diameter. The intensity of each element was measured in counts per second (cps). The elements measured were Si, Ti, Al, Cr, Fe, Mn, Mg, Ni, Ca, K, and Ba.

3.3. Discriminant analysis (DA) using SPSS software

The raw FT-IR spectra of peridotite olivine crystals from this study and that of economic kimberlites from Peslier et al. (2010) and Peslier et al. (2008) were used to discriminate between economic and uneconomic kimberlites using statistical analysis on SPSS software. The raw spectrum normalized to 1 cm⁻¹ thickness were modified using the equations X_{Ti} and X_{Si} below. First, the modification was carried out using the two structural hydroxyl absorbance bands (3572 and 3524 cm⁻¹) associated with the titanoclinohumite-like point-defect (X_{Ti}) because of their presence in all the spectra.

$$X_{Ti} = \frac{X_n - X_{3524}}{X_{3572} - X_{3524}}$$

Following the standardization/modification, the absorbance at all H-associated bands between 3000 cm^{-1} and 3680 cm^{-1} were entered into SPSS software. The band positions used are- $\sim$3228, 3328, 3480, 3524, 3534, 3540, 3590, 3612, 3624, 3638 and 3672. The absorbance at each band position was checked individually to find outliers using a 2-sigma rule, and a total of 47 spectra (8 uneconomic and 39 economic) were ultimately selected for the stepwise discriminant analysis (DA) method. The grouping variable assigned to each spectrum was the economic or uneconomic nature of the kimberlite.

Following DA, the raw spectra were standardized again to include the two structural hydroxyl absorbance bands associated with X_{Ti} and determine their role (if any) in discrimination. The raw spectra were modified using equation X_{Si} for the Si-bands-3612 and 3590 cm^{-1} (associated with H-substitution in Si-vacancy) observed in all the spectra.

$$X_{Si} = \frac{X_n - X_{3612}}{X_{3590} - X_{3612}}$$

The absorbance at all band positions mentioned above (except 3612 and 3590 cm^{-1}) and 3572 and 3524 cm^{-1} were entered into SPSS software, and following outlier determination, a total of 58 spectra (8 uneconomic and 50 economic) were used to carry out multi-step discriminant analysis (DA) again.

4. Results

4.1. Petrography

Most of the studied xenoliths are garnet harzburgites (Table 1) with accessories of chromite, diopside and phlogopite (Fig. 2) with the exception of xenolith-9 which is olivine websterite. The large (> 2 mm) equidimensional-tabular olivine and orthopyroxene grains impart coarse texture. The xenoliths are affected by serpentinization (Fig. 2 f, g) and presence of melt inclusion arrays in olivine and orthopyroxene, which were avoided during FTIR analysis. Garnets have kelyphitic rims of variable size and are often opaque due to intense kelyphitization along cracks (Fig, 2c, d). Compared to the average pyroxene content (20 %) found for the cratonic mantle xenoliths (Pearson et al., 2003), the modal abundance of orthopyroxene is high (> 30 %) in most of studied garnet harzburgites (Table 1) in both the economic and barren kimberlite pipes and can also be used to categorize some of these xenoliths as orthopyroxene-rich (Table 2). In the orthopyroxene-rich xenoliths, the orthopyroxene grains are large and touching compared to those with small and separated orthopyroxene (Fig. 3). The higher orthopyroxene content is ascribed to metasomatism of mantle tapped by all studied kimberlites by hydrous siliceous fluid (Simon et al., 2007; Khan et al., 2024). The xenoliths can be further categorised based on the presence of primary and/or secondary minerals (Tables 1 and 2). Interstitial diopside, chromite, and phlogopite frequently occur as primary grains (Fig. 2 b, e). However, the xenoliths from uneconomic kimberlites also contain a secondary assemblage of phlogopite, Cr-diopside ± chromite which often rims garnet (Fig. 2 c, d), occurs in veins (Fig. 2 f, g), at times forms larger aggregate of Phlogopite, and Cr-diopside ± chromite without garnet (Fig. 2 i). The composition and textures of this secondary assemblage in the veins and around garnets suggest metasomatism and addition of H_2O, CaO, K_2O by a fluid or melt which also causes breakdown of garnet (Khan et al., 2024). This garnet breakdown metasomatism is a unique feature of uneconomic kimberlites and is henceforth used to draw out differences between the kimberlites. The petrography of the selected xenolith thick sec-

tions from the four kimberlites is described in detail below and the calculated modal compositions are presented in Table 1.

4.2. FTIR results

4.2.1. Matsoku

Xenoliths from Matsoku contain a significant amount of 'water', especially in pyroxenes (Table 3). Olivine shows main absorbance bands at $\sim$ 3572, 3591 and 3638 cm^{-1} and additional bands at $\sim$ 3624, 3612, 3534 and 3690 cm^{-1} (Fig. 4 a). The calculated water concentration in olivine for xenoliths 8A and 8B is 24 and 27 ppm respectively (Table 3). Orthopyroxene absorbance bands occur at $\sim$ 3515, 3546, and 3596 cm^{-1} (Fig. 5 a) and wider bands at $\sim$ 3410–3420, 3055–3065 and 3310–3330 cm^{-1}. The calculated water concentration in orthopyroxene (Table 3) for the unmetasomatised xenolith (8A) is 95 ppm and for the xenoliths affected by metasomatism (8B and 9) is 115 and 145 ppm. The clinopyroxene absorbance bands appear at $\sim$ 3639 and 3453 cm^{-1} (Fig. 6 a). Small hydrous mineral bands are found in the spectra at $\sim$ 3682 cm^{-1}, and the water concentration of clinopyroxene in xenolith 8B may be slightly overestimated because of the slight overlap of these bands with H-associated bands. The calculated water concentration in clinopyroxene (Table 3) is between 87 and 460 ppm, with the lowest water concentration in the 8A xenolith, which has primary garnet unaffected by metasomatism.

4.2.2. Thaba Pustoa

The highest absorbance band in olivine is at $\sim$ 3572 cm^{-1} (Fig. 4 b), followed by those at $\sim$ 3591, 3638 and 3624 cm^{-1}. Additional absorbance bands of less intensity are at $\sim$ 3612, 3540, and 3523 cm^{-1}. The 16A xenolith shows higher absorbance than the 16B xenolith (Table 3) giving water concentration in olivine of 30 and 25 ppm wt. respectively. Both Thaba Putsoa xenoliths are affected by metasomatism, but show olivine water concentrations similar to those of Matsoku xenoliths (Table 3). They differ from Matsoku xenoliths in showing no hydrous phase absorbance band. Orthopyroxene bands in Thaba Putsoa xenoliths occur at $\sim$ 3515 and 3546 cm^{-1} (Fig. 5 b), with low-intensity bands at $\sim$ 3590 cm^{-1}. Similar to Matsoku xenoliths, wider bands occur in orthopyroxene at $\sim$ 3400–3420, 3055–3085 and $\sim$ 3295–3330 cm^{-1} and the band at $\sim$ 3055–3085 cm^{-1} has higher intensity. The band at 3688 cm^{-1} (Fig. 5 b), representative of hydrous minerals, affects the 16-A xenoliths and is subtracted (excluded) from the water concentration calculation. The estimated water concentration in orthopyroxene is 125 and 230 ppm wt. for xenoliths 16A and 16B, respectively (Table 3). The primary clinopyroxene in xenolith 16B shows serpentine absorption bands, and the water concentration could not be determined.

4.2.3. Pipe 200

The xenoliths 29A and 29B, affected by metasomatism, show different intensity of the olivine absorbance bands in comparison to the 32B and 32C xenoliths, unaffected by metasomatism. The olivine absorbance band at $\sim$ 3571 cm^{-1} shows the highest intensity in all Pipe 200 xenoliths (Fig. 4 c), with relatively lower intensity in 32B and 32C compared to 29A and 29B. Other major and minor bands in all xenoliths are $\sim$ 3591, 3638 and 3624 and, 3612 and 3534 cm^{-1}. Xenoliths 32B and 32C, affected by metasomatism, show additional major bands in olivine at $\sim$ 3672 and 3535 cm^{-1} (Fig. 4 c). The Pipe 200 xenoliths show a relatively large range in the olivine water concentration (Table 3), which varies between 33 to 27 ppm in 29A and 29B respectively and 20 to 17 ppm calculated from 32B and 32C xenoliths which show garnet breakdown assemblage (Table 1). The orthopyroxene absorbance bands (Fig. 5 c) in Pipe 200 xenoliths occur at $\sim$ 3516, 3546, 3600 cm^{-1}, wider bands at $\sim$ 3410–3420, $\sim$3055–3065 cm^{-1},
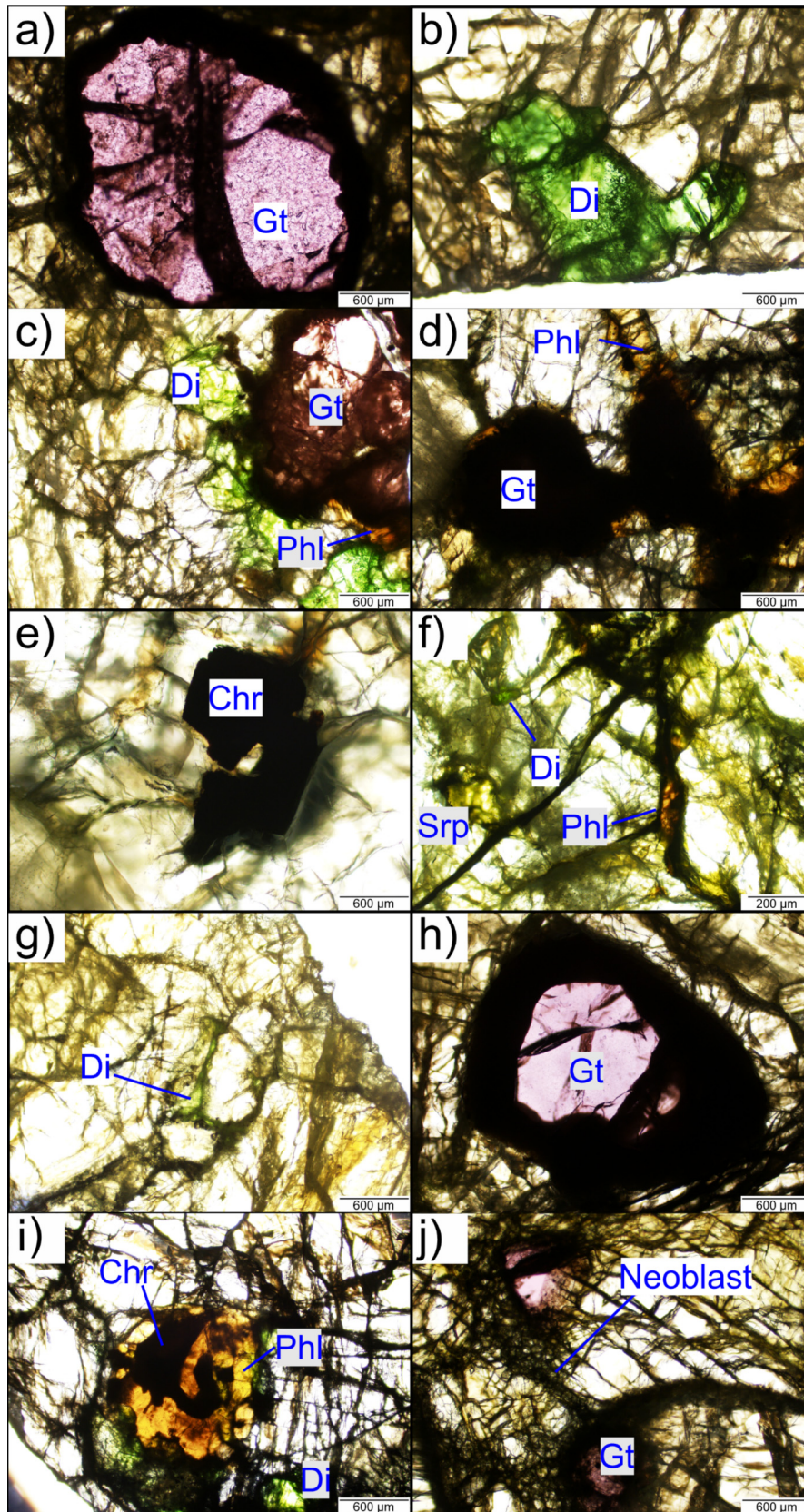
Fig. 2. Microphotographs of the textures in the studied xenoliths from Lesotho and South African kimberlites: (a, b) 8A, primary garnet and chrome-diopside; (c) 9, garnet surrounded by metasomatic breakdown assemblage of phlogopite and chrome-diopside; (d) 16B, garnet surrounded by phlogopite; (e) 16B, primary chromite; (f) 16A, phlogopite and diopside in metasomatic vein assemblage; (g) 32B, bright green diopside along the veins and rims olivine; (h) 29B, primary garnet with thick kelyphitic rim; (i) 32C, metasomatic garnet breakdown products of chromite, phlogopite and chrome diopside; (j) 55, olivine neoblasts in sheared xenolith showing porphyroclastic texture.
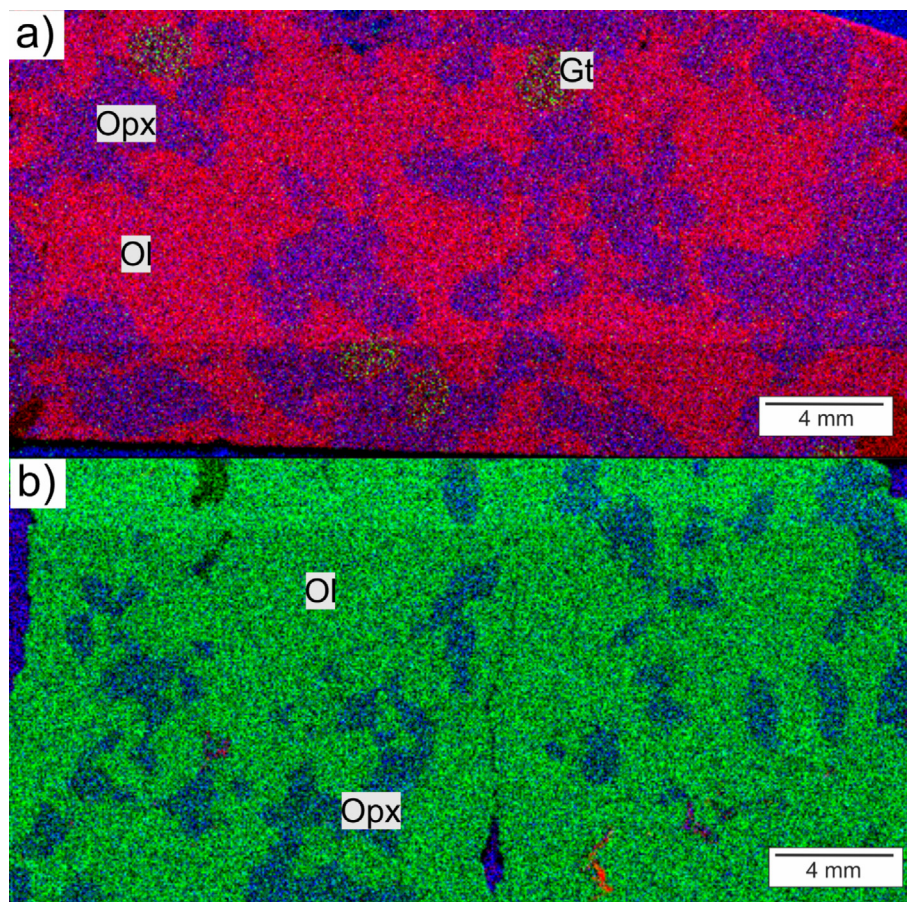
Fig. 3. XRF spectroscopy major element distribution map for xenolith A) 29-A showing orthopyroxene rich (R: G: B- Fe: Al: Si) and B) 32-B- showing orthopyroxene poor (R: G: B- Ca: Fe: Si) harzburgite. The R: G: B sequence for the elements is given in the brackets. Ol- olivine, opx- orthopyroxene, gt- garnet.

and minor bands at $\sim$ 3310–3330 cm^{-1}. Orthopyroxene spectra of all Pipe 200 xenoliths have hydrous mineral bands at $\sim$ 3685–3690 cm^{-1}, and its removal in water content calculation may underestimate the orthopyroxene water content due to slight overlap. The calculated water content in orthopyroxene is 21–92 ppm (Table 3). The clinopyroxene absorbance bands appear at $\sim$ 3636 and 3446 cm^{-1} (Fig. 6 c). with an additional minor band at $\sim$ 3648 cm^{-1} in xenolith 29B. Small hydrous mineral bands occur in the clinopyroxene spectra (Fig. 6 c) at $\sim$ 3690 and 3680 cm^{-1} in 29-B and 29-C xenoliths. The calculated water concentration in clinopyroxene in 29B xenolith may be overestimated compared to a smaller band in 32C xenolith, where the water concentration may be slightly overestimated. The calculated water concentration in clinopyroxene (Table 3) is 737 and 833 ppm for xenolith 29B and 32C, respectively.

4.2.4. Bultfontein

The highest band intensity in olivine is at $\sim$ 3571 cm^{-1} (Fig. 4 d). Other major olivine absorbance bands include $\sim$ 3590, 3612, 3624, 3638, 3524, and 3540 cm^{-1} (Fig. 4 d). In addition to Group (1) absorbance bands, xenolith 51 shows a broad band between $\sim$ 3224–3228 cm^{-1}. The minor bands in both xenoliths are at $\sim$ 3500, 3476, 3463 and 3685 cm^{-1} and in the Group (2) region (3450–3100 cm^{-1}) at $\sim$ 3328, 3370, 3228 and 3405 cm^{-1}. Bultfontein xenolith olivines have the highest water concentration in this study. The calculated water concentrations in olivine (Table 3) from xenoliths 51 and 55A are 41 and 62 ppm respectively. The orthopyroxene absorbance bands in Bultfontein xenoliths occur at $\sim$ 3514, 3546, and 3600 cm^{-1} (Fig. 5 d) and wider

bands at $\sim$ 3310–3330, 3410–3420 and 3055–3065 cm^{-1}. Amongst the low-intensity bands, the band at 3055–3065 cm^{-1} has a higher intensity in xenolith 51. The xenoliths show the hydrous mineral bands at $\sim$ 3685–3690 cm^{-1} and $\sim$ 3678 cm^{-1} (Fig. 5 d). Their removal may slightly underestimate the orthopyroxene water content calculation giving 176 and 60 ppm (Table 3). The clinopyroxene absorbance bands in xenolith 51 appear at $\sim$ 3648 and 3450 cm^{-1} (Fig. 6 d). The band at $\sim$ 3684 cm^{-1} is due to the hydrous phase, and the calculated clinopyroxene water concentration (Table 3) of 604 ppm wt. may be overestimated.

4.3. Statistical analysis of olivine spectra

In the case of structural hydroxyl absorbance bands after X_{Ti} standardization, the multi-step discriminant analysis identifies 3638 cm^{-1} as the best discriminator of economic and uneconomic kimberlite. In subsequent steps, bands at 3624 and 3672 cm^{-1} are identified. The results of the DA$_{Ti}$ are considered acceptable based on eigenvalue (1.5) and canonical correlation (0.775). Equation (1) was obtained from DA$_{Ti}$ where A^{3638}, A^{3672}, and A^{3624} are structural hydroxyl absorbance bands at 3638, 3672, and 3624 cm^{-1} respectively. The analysis results can also be seen in the histogram in Fig. 7a, which shows a good separation between economic and uneconomic kimberlites, with the economic kimberlites having lower scores and the uneconomic kimberlites having higher scores.

$$Da_{Ti} = -4.851 * A^{3624} + 8.606 * A^{3638} - 2.659 * A^{3672} - 0.201$$
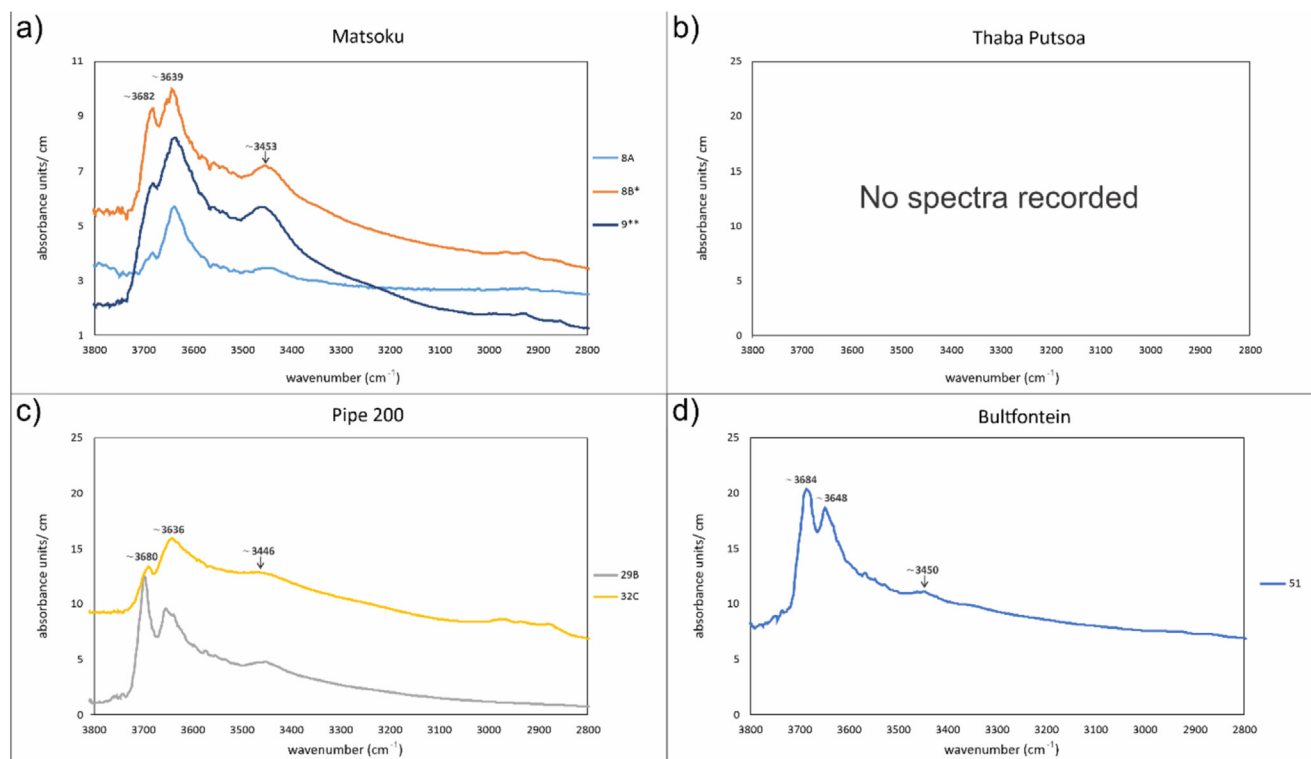
(1)
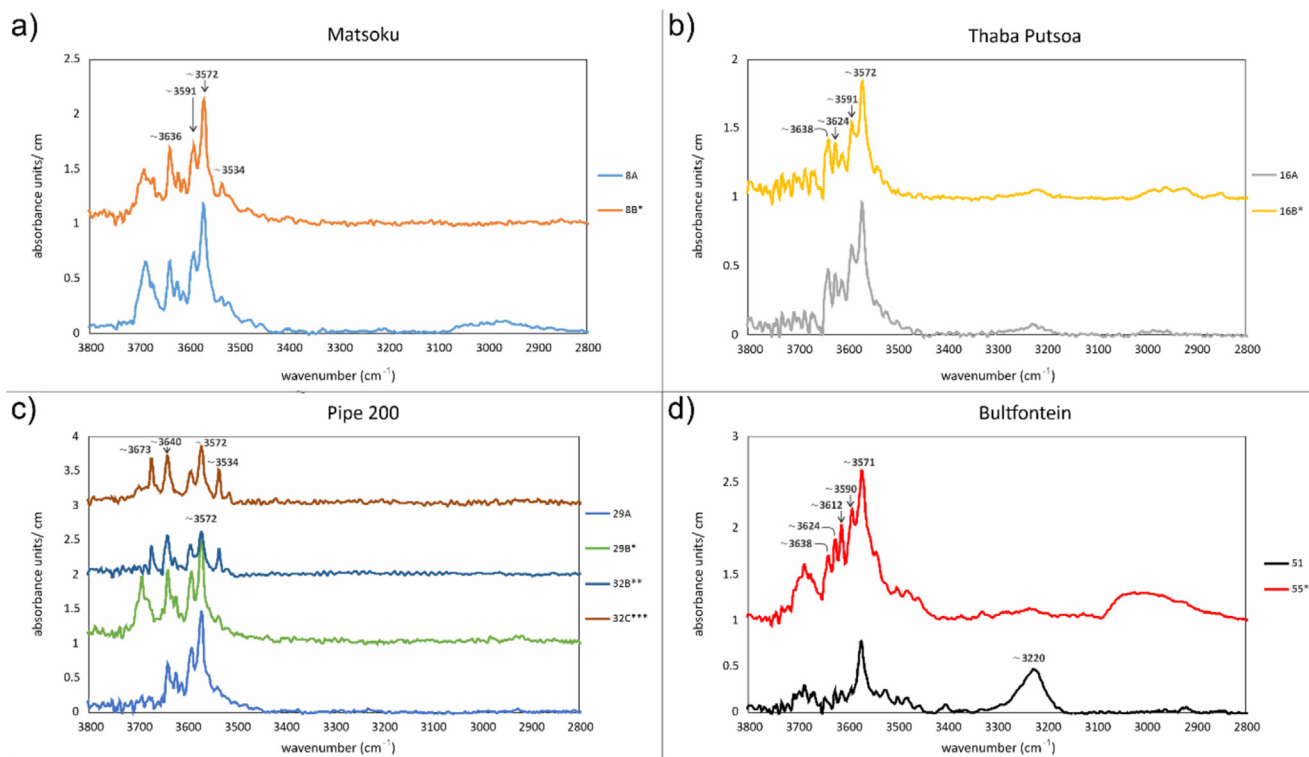
Fig. 4. Representative average unpolarized infrared spectra for olivine in the studied xenoliths. Absorbance units are normalized to 1 cm thickness. The spectra are shifted for clarity where * = addition of 1 absorbance unit.
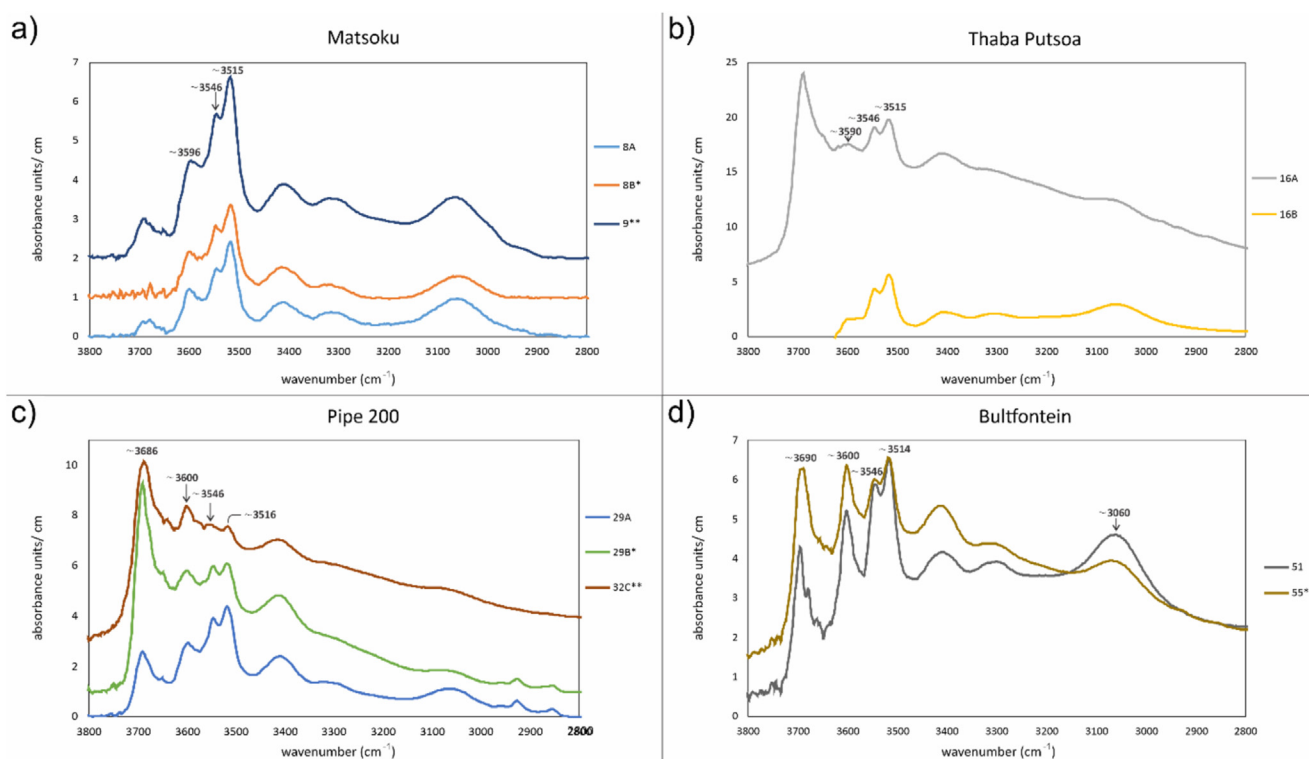
Fig. 5. Representative average unpolarized infrared spectra for orthopyroxene in the studied xenoliths. Absorbance units are normalized to 1 cm thickness. The spectra are shifted for clarity where * = addition of 1 absorbance unit.

Similarly, for the X_{Si} standardized structural hydroxyl absorbance bands, discriminant analysis identifies the 3638 and 3540 cm^{-1} bands as discriminators of economic and uneconomic kimberlites.

After the multi-step DA_{Si}, equation (2) is obtained where A^{3638} and A^{3540} are structural hydroxyl absorbance bands at 3638 and 3540 cm$^{-1,}$ respectively. The difference can also be seen in the his-

Fig. 6. Representative average unpolarized infrared spectra for clinopyroxene in the studied xenoliths. Absorbance units are normalized to 1 cm thickness. The spectra are shifted for clarity where * = addition of 1 absorbance unit.

togram in Fig. 7b, where uneconomic kimberlites have higher discriminant scores and economic kimberlites have a lower score.

The separation between the economic and uneconomic kimberlites shows slight overlap, but the eigenvalue of 0.989 and the canonical correlation of 0.705 suggest still good separation.

$$Da_{Si} = -0.903 * A^{3540} + 1.389 * A^{3638} - 0.596 \qquad (2)$$

5. Discussion

5.1. Interpretation of infrared spectra

The four commonly found OH⁻ substitution mechanisms in olivine associated with (1) Si vacancies, (2) Mg vacancies, (3) Ti, and (4) trivalent cations are commonly labeled as [Si], [Mg], [Ti], and [triv]. The distinct O-H stretching modes observed in the infrared spectrum detailed in Kovács et al. (2010) are absorption bands between 3630 and 3400 cm⁻¹ for [Si], 3400 and 3300 cm⁻¹ for [triv], 3300 and 3100 cm⁻¹ for [Mg] and two prominent absorption peaks at 3572 and 3525 for [Ti].

In this study, the olivine absorbance bands associated with the Ti-clinohumite [Ti] and Si vacancies [Si] at ∼ 3523, 3572 and ∼ 3540, 3591, 3612, 3624, 3638 cm⁻¹ (Jollands et al., 2018; Kovács et al., 2010, and references therein) are present in xenoliths from all four pipes (Fig. 4). The [Ti] absorbance band at ∼ 3572 cm⁻¹ occurs in Ti-doped experiments (Kovács et al., 2010) but the other band at 3525 cm⁻¹ is absent in our samples. These absorbance bands between 3650 and 3450 cm⁻¹ are commonly referred to as Group I bands. Olivine from Thaba Putsoa (16-A and 16-B) and Bultfontein (51) xenoliths also show a broad low absorption band at ∼ 3220 cm⁻¹ (Fig. 4 b and d) associated with [Mg] − the substitution of a divalent cation (usually Mg) by two H⁺ (Berry et al., 2005). The absorption bands between 3450

and 3100 cm⁻¹ are commonly referred to as Group II bands. The [Mg] absorbance band at ∼ 3220 cm⁻¹ in olivine occurs in enstatite-buffered experiments, and its dominance in Bultfontein xenoliths suggest Mg-rich (Fo-rich) olivine in equilibrium with orthopyroxene (Peslier and Luhr, 2006). However, Kovács et al. (2012) suggest that another reason for ∼ 3220 cm⁻¹ band could be dominance of [Si] and [Mg] due to high f_{H2O}. Interestingly, olivine from Pipe 200 xenoliths (32B and 32C), affected by metasomatism, show the band at ∼ 3672 cm⁻¹ (Fig. 4c) associated with inclusion of talc (Hilchie et al., 2014; Koch-Müller et al., 2006; Matsyuk and Langer, 2004). Absorbance bands at ∼ 3687−−3690 c m⁻¹ corresponding to hydrous phase are common in the olivine spectra of Matsoku, Pipe 200 and Bultfontein xenoliths (Fig. 4 a, b and c). The FTIR spectra band for lizardite (3687 and 3644 cm⁻¹) and chrysotile (3693 and 3647 cm⁻¹) in this study are similar to those obtained in Liptai et al. (2023), but the band at ∼ 3645 is absent.

The orthopyroxene spectra have the same band positions and show the presence of serpentine for xenoliths from all four pipes where the intensities of the spectra vary between the pipes. The major absorbance bands in the studied orthopyroxene are at wavenumbers greater than 3400 cm⁻¹ at ∼ 3515, 3546, 3596 cm⁻¹ (Fig. 5). They are associated with the linked substitution of hydroxyl and trivalent cations (Al, Cr, etc.) in the orthopyroxene structure (Prechtel and Stalder, 2012; Stalder and Skogby, 2003). The exact hydroxyl substitution method for the orthopyroxene structure is not well known because of the complex structure of orthopyroxene and limited research on the topic. However, Yang et al. (2021) shed light on the hydrogen defects in orthopyroxene during high-temperature processes and demonstrated that the bands at ∼ 3515 and 3546 cm⁻¹ are ascribed to hydrogen linked to Al in Si vacancies due to the presence of these bands in the synthetic orthopyroxene. However, the band at ∼ 3546 cm⁻¹ in xenoliths from all four pipes is uncommon and is rare in natural mantle
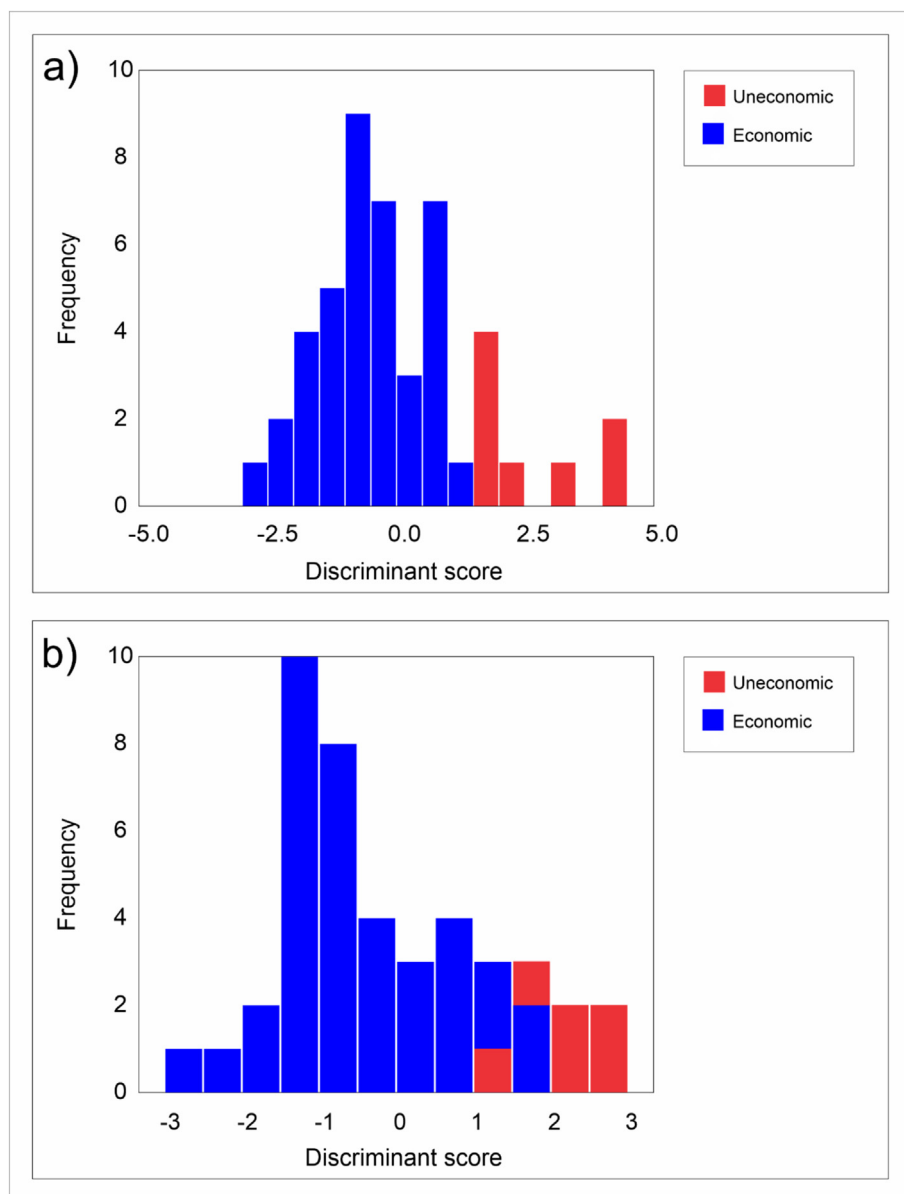
Fig. 7. Results of the discriminant analysis (DA) shown as histogram a) DA_{Ti} and b) DA_{Si} based on the discriminant score. The separation between economic and uneconomic kimberlites is good using X_{Ti} and reasonable using X_{Si} due to the overlap in the middle.

orthopyroxenes. Yang et al. (2021) suggest the possible formation of these bands from inter-site reaction without any association with fluid or melt. The band at ~ 3590 cm^{-1} is associated with hydrogen substitution in the Si vacancy defect (Prechtel and Stalder, 2011) and is most prominent in xenoliths of economic Bultfontein kimberlite (Fig. 5d), which are not metasomatized. The broader absorbance bands are present in orthopyroxene from all studied xenoliths at ~ 3410–3420, 3055–3065, and 3310–3330 cm^{-1}. The band at ~ 3410–3420 cm^{-1} corresponds to the redistribution of ferrous iron from the M1 to M2 sites (Stalder and Skogby, 2007). Yang et al. (2021) suggest that the ~ 3410–3420 cm^{-1} absorbance band form due to the later incorporation of hydrogen at the relevant M site. Similar to olivine, the band related to hydrogen defects in Mg vacancies at 3055–3065 cm^{-1} (Fig. 5d) is prominent in the Bultfontein xenolith (51). The broad band at 3310–3330 cm^{-1} shows the lowest absorbance in all the xenoliths. Similar to olivine, the hydrous phase absorbance bands occur in orthopyroxene at higher wavenumbers (~ 3685–3695 cm^{-1}) and

correspond to the serpentine group minerals lizardite and chrysotile (Madejová et al., 2017). In Bultfontein xenolith (51), the orthopyroxene spectra show an additional band for amphibole at ~ 3678 cm^{-1} (Liptai et al., 2023). The equilibration criteria of orthopyroxene water activity (higher or lower) based on the intensity of the bands at ~ 3600, ~ 3525 and ~ 3420 cm^{-1} developed by Patkó et al. (2019) can only be applied with reservation to the orthopyroxene spectra from this study because (i) the ~ 3523 cm^{-1} absorbance band is shifted to ~ 3515 cm^{-1}, (ii) presence of an additional band at ~ 3546 cm^{-1}, (iii) the methodology is developed for spinel peridotites from a young extensional Miocene basin (i.e. the Pannonian basin in central Europe).

The absorbance bands in Matsoku and Pipe 200 xenolith clinopyroxenes occur at ~ 3638 cm^{-1}, followed by those at 3453 cm^{-1} (Fig. 6). Identification of hydroxyl substitution in clinopyroxene is less clear than for orthopyroxene (Patkó et al., 2019). However, similarly to orthopyroxene, hydroxyl is coupled to Al^{3+} and is incorporated in the vacancies (O'Leary et al., 2010).

The highest intensity band at $\sim$ 3638 cm^{-1} may be associated with Si-vacancies filled by hydrogen ions or the coupled substitution of Na$^+$ and H$^+$ in the M2 site during ferric iron reduction (Bromiley et al., 2004; Stalder and Ludwig, 2007). The band at $\sim$ 3450 cm^{-1} is assigned to structural hydroxyl in the octahedral vacancy (M2) and is correlated with the Ca-Eskola component (Kovács et al., 2016, and references therein). The band at $\sim$ 3520 cm^{-1} commonly observed in mantle xenoliths and experimentally synthesized samples and assigned to the H$^+$ charge-balancing substitution of Al^{3+} into the tetrahedral Si site (Koch-Müller et al., 2004) is absent in our samples. The absorbance band at $\sim$ 3638 cm^{-1} (Fig. 6d) is replaced by $\sim$ 3648 cm^{-1} band in clinopyroxene from Bultfontein pipe xenolith (51). The hydrous phase band appears in clinopyroxene as a broad ($\sim$3680−−3690 cm^{-1}) band in all xenoliths except for one xenolith (29-B) from Pipe 200, where the serpentine band occurs at $\sim$ 3695 cm^{-1}. It is assigned to the presence of amphibole lamellae and serpentine (Della Ventura et al., 2007). The highest intensity band at $\sim$ 3638 cm^{-1} is similar to that of type 1 clinopyroxene in the classification of Patkó et al. (2019) and is suggested to represent equilibrium conditions after partial melting or metasomatic events and may indicate equilibration at higher water activity. As we discussed for orthopyroxene, the classification of Patkó et al. (2019) may not be directly applied in our case.

The FTIR bands in xenoliths from the studied pipes suggest differences in the OH$^-$ substitution mechanisms between the pipes and hints to metasomatism. The olivine absorbance bands indicate the presence of Ti-clinohumite and Si vacancies, common across all xenoliths. Additionally, distinct bands at $\sim$ 3220 cm^{-1} may suggest Mg-deficient, and therefore higher Si-activity olivines, particularly in Bultfontein xenoliths. In orthopyroxene, the presence of serpentine and varying band intensities across different pipes highlight the complexity of hydrogen incorporations and cation substitutions. Bands at $\sim$ 3515, 3546, and 3590 cm^{-1} indicate coupled hydroxyl and trivalent cation substitutions, with variations reflecting different metasomatic histories. Clinopyroxene spectra similarly show coupled hydroxyl and aluminum substitution in aluminum vacancies, with $\sim$ 3638 cm^{-1} bands probably associated with equilibrium conditions after metasomatism or partial melting. Overall, these FTIR bands reveal the effects of metasomatism and mineralogical differences between the xenoliths from different pipes.

5.2. Comparison of water contents

The water concentrations in olivine in the studied xenoliths is 17–62 ppm (Table 3). This is within the 86 ppm previously reported by Peslier et al. (2010) for mantle peridotites from Kaapvaal craton kimberlites and significantly lower than concentrations of up to 357 ppm reported by Jackson and Gibson (2023) for mantle peridotite xenoliths from Bultfontein and Mothae kimberlites. The highest olivine water concentrations in this study (41 and 62 ppm) were measured in the economic Bultfontein kimberlite (Fig. 6d), located in the interior of the craton (Fig. 1). In the uneconomic pipes from Northern Lesotho, the water concentration in olivine (Table 3) is lower in the xenoliths affected by metasomatism (with the garnet breakdown assemblage) (17–30 ppm) and slightly higher in the xenoliths containing primary intact garnet (27–33 ppm). The lower olivine water content hints at dehydration during metasomatism by water-poor and CO$_2$-rich melts or fluids (Sokol et al., 2013; Doucet et al., 2014). The profiles of water content across olivine grains from this study are flat and do not show any enrichment in H defects in olivine core in a form of bell-shaped curves as reported for olivines in the Kaapvaal Craton kimberlite xenolith (Hilchie et al., 2014; Peslier et al., 2008). The flat shape of H profiles combined with the low olivine water concentration indicates diffusive water loss during metasomatism.

The orthopyroxene water concentration in the xenoliths from this study covers a large range (21–230 ppm) (Table 3) like the range of 40–250 ppm reported in Peslier et al. (2012) and 27–285 ppm reported in (Jackson and Gibson, 2023). The water concentrations in pyroxene from uneconomic kimberlites from Northern Lesotho show an opposite trend to that shown by olivine. The water concentration in orthopyroxene is higher in the xenoliths affected by the metasomatism (garnet showing replacement assemblage of Chr + Phl + Cpx) and lower in the xenoliths with primary garnets (Table 3), except for the orthopyroxene from 32-C xenolith (Pipe 200). However, our calculated water concentration in orthopyroxene may be underestimated due to the removal of serpentine absorbance bands (Table 3, in bold) which can explain the lower water concentration of orthopyroxene from xenolith 32-C as well as overall lower water contents for Pipe 200 orthopyroxene. One possible reason for the observed discrepancy between water content and metasomatism in olivine and orthopyroxene could be due to pyroxenes preserving their original mantle water content much better than olivine (Bell and Rossman, 1992; Grant et al., 2007) but the faster diffusion-driven water loss in olivine as compared to orthopyroxene during kimberlite ascent cannot be overlooked. In addition, the nature of the metasomatic agent can also play a role. For example, Al affects the incorporation of hydrogen in orthopyroxene and the partitioning of hydrogen between orthopyroxene and olivine (Demouchy and Bolfan-Casanova, 2016, and references therein). Consequently, Al-rich orthopyroxene or possible metasomatism involving fluid/melt rich in Al will affect the hydrogen concentration of the minerals, likely increasing the hydrogen content in orthopyroxene under high-Al conditions. The higher orthopyroxene water content of xenoliths affected by metasomatism (Table 3), compared to that in garnet harzburgites, support this observation.

Similar to orthopyroxene, the water concentration in clinopyroxene is lower in the xenoliths with primary garnets. Clinopyroxene water concentration for the xenoliths in this study covers a wider range (87–833 ppm) (Table 3) than the previously reported 15–400 ppm and 70–300 ppm in Peslier et al. (2012) and Jackson and Gibson (2023), respectively. Inclusions of serpentine and amphibole lamellae bands may result in overestimation of the clinopyroxene water concentration in the case of 29B and 51 (Table 3, in bold).

Comparing only the xenoliths unaffected by metasomatism (i.e., with primary garnet) shows that the ones from economic Bultfontein kimberlites have higher water concentration in olivine and orthopyroxene (Table 3). It has been previously demonstrated for the Kaapvaal Craton, that the xenoliths from the interior of the craton are more hydrated than those from the margin (Jackson and Gibson, 2023; Peslier et al., 2010). However, it is unclear whether it plays any role in affecting diamond grade.

The partition coefficient of water between orthopyroxene and olivine ($D_{H2O}^{opx/ol}$) calculated for the studied xenoliths can reach up to 9.11 with an average of 3.60 ± 2.34. It is higher than 1.6 ± 0.2 and 0.61 calculated by Bell et al. (2004) and Withers et al. (2011) for Kaapvaal Craton megacrysts and is closer to the $D_{H2O}^{opx/ol}$ 4.5 measured by Peslier et al. (2012). The higher measured $D_{H2O}^{opx/ol}$ could be due to (i) the addition of water to orthopyroxene, (ii) loss of water from olivine, or (iii) both processes. While olivine inclusions in diamonds are typically dry (Matsyuk and Langer, 2004; Novella et al., 2015), the olivines from ambient mantle peridotite xenoliths contain significant amount of water explained by the hydration of xenolithic olivines by later-stage water-rich silicate or fluid metasomatism (Novella et al., 2015). If a closed system is considered, hydrogen is transferred from olivine to pyroxene with increasing pressure (Mierdel et al., 2007). However, in the current case, the olivine water concentration is at the lower end of that in literature, moreover, the calculated inter-mineral water partition coefficient

$D_{H2O}^{opx/ol}$ is high. This could be due to the addition of water to orthopyroxene from an Al-rich metasomatic agent which would promote the uptake of hydrogen into orthopyroxene. In addition, a loss of water from the olivine to the metasomatic agent or diffusion of hydrogen during uplift to the kimberlite melt could also explain high $D_{H2O}^{opx/ol}$ in our samples. The first process involving an addition of water is supported by the signatures of metasomatism by water-poor and CO_2-rich melt causing garnet breakdown metasomatism as observed in the studied xenoliths. However, the xenoliths unaffected by metasomatism (with primary garnets) also have lower water content in olivine and higher in orthopyroxene (Table 3). Loss of hydrogen from olivine during re-equilibration with metasomatic agent or kimberlite melt is supported by the flat hydrogen profiles and low integrated absorbance in olivines from this study as compared to the bell-shaped hydrogen diffusion profiles recorded for the same xenoliths by Hilchie et al. (2014).

In conclusion, the study reveals that the water content in olivine and orthopyroxene from xenoliths is significantly influenced by metasomatism and the nature of the metasomatic agent plays a significant role. Overall, the water concentration in olivine and orthopyroxene in xenoliths affected by metasomatism suggests diffusion-driven dehydration of olivine by water-poor melts (or fluids) during the kimberlite ascent or in the mantle source. The addition or better retention of orthopyroxene water in this study is influenced by Al content. The calculated water partition coefficient between orthopyroxene and olivine ($D_{H2O}^{opx/ol}$) is higher in all xenoliths, potentially due to the loss of water from olivine during kimberlite ascent.

5.3. Interpretation of Kaapvaal Craton kimberlite xenolith water concentration

The water concentration of NAMs in the xenoliths from the Kaapvaal Craton kimberlites in this study (Table 3) is compared to that in the literature in the Supplementary data- Table 1. The estimates for the formation pressure of the xenoliths (where available) vary in the range of 2.5–7 GPa. Most xenoliths from economic kimberlites show low water contents in olivine and variable water concentration in orthopyroxene (Supplementary data- Table 1). Intriguingly, most xenoliths with formation pressure 5 GPa or higher have low water concentration in olivine. These low water concentrations of olivine derived from greater depth may indicate "dry" melt metasomatism events at the base of the Kaapvaal Craton lithosphere (Doucet et al., 2014; Peslier et al., 2010). Furthermore, xenoliths from this study showing evidence of garnet breakdown during metasomatism have lower olivine water concentration (Table 3) than those with primary garnets. The xenoliths from uneconomic kimberlites in this study show an intermediate olivine water concentration at low orthopyroxene water concentration (Table 3; Supplementary data- Table 1). The water concentration in both olivine and orthopyroxene from uneconomic kimberlite xenoliths is also lower than that from economic kimberlite xenoliths which equilibrated at lower formation pressures.

Our study shows the lower olivine and orthopyroxene water concentrations in the xenoliths from uneconomic kimberlites at the edge of the craton. Jackson and Gibson (2023) previously found that the xenoliths from the margin of the Kaapvaal Craton are less hydrated than those from the interior. In our study, the examples of xenoliths from uneconomic kimberlite are limited to those from the margin of the Kaapvaal Craton (Fig. 1), which did not allow us to examine how the different styles of metasomatism affected the water concentration in xenoliths from uneconomic kimberlites from the craton margin and interior. A detailed study with a larger dataset of kimberlites with variable diamond grades and locations around the craton would be necessary.

5.4. Using statistical analysis to determine the nature of hydrogen substitution between economic and uneconomic kimberlites

The standardization of olivine spectra using structural hydroxyl absorbance associated with different bands in the olivine structure offers two approaches to differentiate between the economic and uneconomic kimberlites. The standardization using Ti-clinohumite point defect (X_{Ti}) related bands for standardization results in 100 % predicted group membership for both economic and uneconomic kimberlites and using Si bands results in 100 % and 84.2 % predicted group membership verification for the uneconomic and economic kimberlites, respectively. Application of the discriminant analysis to these two standardizations classified the economic and uneconomic kimberlites in Fig. 8. For X_{Ti} standardization, the absorbance in olivine from uneconomic kimberlites (Fig. 8a) have higher A_{3638} band absorbance at lower A_{3540} band absorbance, while olivine from economic kimberlites shows large variation in absorbance with overall lower A_{3638} band absorbance at higher A_{3540} band absorbance. Despite a small overlap, the separation between economic and uneconomic kimberlites is very good (Fig. 8a). The X_{Si} standardization shows a large range and positive correlation for A_{3638} and A_{3624} band absorbance (Fig. 8b) in olivine for economic kimberlites and a narrow clustering of absorbances for the uneconomic kimberlites.

The olivine structural hydroxyl absorbance bands identified in equation (1) and (2) (3540, 3624, 3638 and 3672 cm^{-1}) are at the upper limit of hydrogen-associated high wavenumber region and their substitution mechanism is ambiguous as discussed below.

The Ti band at 3525 cm^{-1} is largely absent in our samples (Fig. 4). Perhaps because Ti defects are common for mantle olivines from spinel peridotite (Berry et al., 2005), whereas our samples are mainly garnet (or garnet spinel) peridotites. However, the dominant band at 3572 cm^{-1} in all samples does not affect statistical discrimination.

Olivine from uneconomic kimberlites shows very strong Group I hydroxyl absorbance bands (Fig. 4). In contrast, the Group II structural hydroxyl absorbance bands are largely absent or weak and do not play a role in the discrimination. The abundance of Group I H$^+$-associated bands in our samples suggests that the olivines have high concentration of Si vacancies (Kovács et al., 2010). Absence of Ti-related OH band at 3525 cm^{-1} (Fig. 4) in Ti-bearing olivine is associated with equilibration of olivine with low silica activity media, indicating equilibration with low silica activity aqueous fluid rather than a melt (Yang, 2016). The H$^+$ substitution mechanism for bands at 3540, 3624, 3638, and 3672 cm^{-1} (in equations (1) and (2) of the discriminant analysis is not well defined.

The high-pressure experiments with peridotite in F ± TiO$_2$ −bearing systems by Fabbrizio et al. (2013) produced absorbance bands at ∼ 3535, ∼3595, 3640 and 3670 cm^{-1} which are close to 3540, 3638 and 3672 cm^{-1} bands identified with our discriminant analysis. The 3624, 3638, and 3672 cm^{-1} bands in our study are close to the 3620, 3637 and 3668 cm^{-1} bands in the olivine spectra of Kaapvaal craton kimberlites from Mosenfelder et al. (2011) interpreted to be due to H sites affected by nearby F and/or B. Similarly, Matsyuk and Langer (2004) assign bands at 3538 and 3672 cm^{-1} to boron-related defects. The interpretation of boron-associated substitution of H sites is often based on the identification of the 3672 cm^{-1} band in B and F-containing olivine in Skyes et al. (1997). However, these bands are not identified in the coupled substitution of B and H in olivine in the experimental study by Ingrin et al. (2014) who demonstrate that these bands rather represent a coupled substitution of H with F. While the association of 3640 cm^{-1} band with halogens (Fabbrizio et al., 2013) is a compelling evidence towards metasomatism, other studies con-
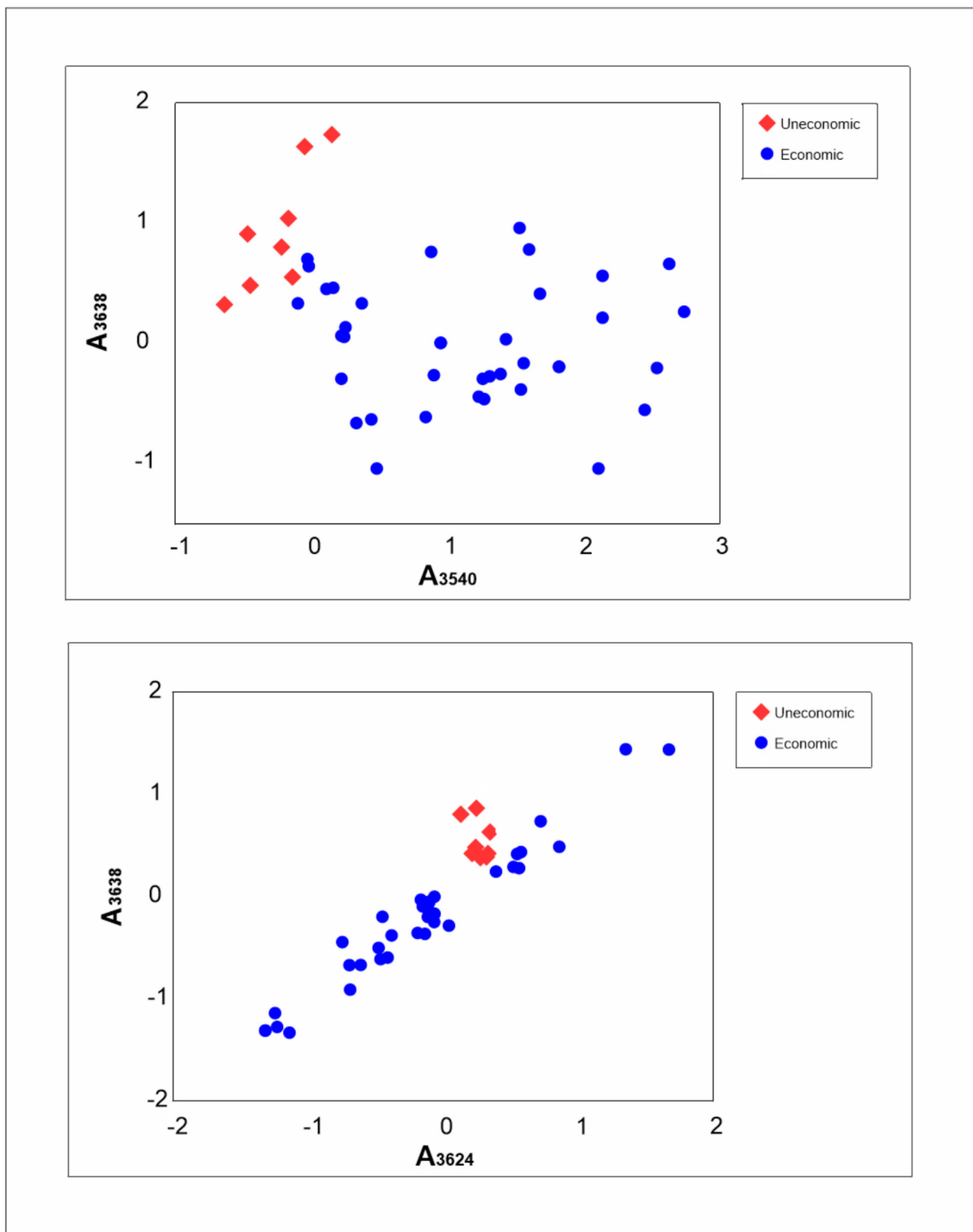
Fig. 8. Scatter plot of the olivine structural hydroxyl band absorbance after standardization showing the separation between uneconomic (red rhombus) and economic (blue circle) kimberlites. A) 3638 vs. 3540 band absorbance after X_{Ti} standardization; B) 3638 vs. 3624 band absorbance after X_{Si} standardization.

sider this absorbance band to be associated with Si-vacancies (e.g., Yang, 2016). Beran and Libowitzky (2006) assign it to serpentine with the possible planar OH-bearing defects. Similarly, a band at 3674 cm^{-1} is also observed in the spectra of forsterite from Pamir

and is interpreted to represent an inclusion of phyllosilicate mineral (Chukanov and Chervonnyi, 2016, and references therein). Lastly, the 3624 cm^{-1} band is associated with Si-related vacancy (Balan et al., 2011; Blanchard et al., 2017). However, occurrence

of the 3695 cm^{-1} band in pyroxene in Liptai et al. (2023) suggests to form due to replacement of adjacent olivine and representing secondary weathering products such as smectite when accompanied by higher wavenumber bands > 3690 cm^{-1} (not included in the statistical analysis). Thus, the possibility of hydrous defects related to hydrous phases, such as serpentine or talc and clay minerals cannot be ruled out for this band.

The 3638 cm^{-1} band is the most significant in the discriminant analysis as it takes part in both modifications. This band is identified in the F-rich olivine along with the 3672 cm^{-1} band (Fabbrizio et al., 2013; Mosenfelder et al., 2011) and in the experimentally hydrated Fe-bearing olivines over variable pressures of 0.3–7GPa and 900–1300 °C temperature (Yang, 2016, and references therein). An experimental study of the substitution mechanisms of H in olivine at 1050 °C and 3 GPa by Tollan et al. (2017), observed a band around 3638 cm^{-1} in association with trivalent cations (Sc-doped) at the highest water activity and the strongest absorbance in spectra measured parallel to principal crystallographic axis'a'. While the band around 3638 cm^{-1} is present in the spectra of olivine from both economic and uneconomic kimberlites, its dominance in uneconomic kimberlites (Fig. 4a, 4b and 4c) may suggest a similar increase in the water activity which may increase oxygen fugacity (Feig et al., 2010). Moreover, the increased water activity can also impact diamond habit (i.e. fibrous or octahedral) (Smith et al., 2015).

Although the exact nature of the identified bands could not always be clearly identified, they point towards metasomatism. The applied statistical analysis highlights the role of Si-related defects over the limited control of other commonly found defects (Mg, Ti, and trivalent cation) in the diamond potential of kimberlite. Metasomatic and/or alteration-associated processes play a greater role in the modification of olivine and other NAMs. The 3638 cm^{-1} band suggests stabilization at high water activity and oxygen fugacity.

In summary, the mode and concentration of structural hydroxyl incorporations in the olivine structure shows the difference between the economic and uneconomic kimberlites. The two suggested approaches prove to be effective in distinguishing the kimberlites in the Kaapvaal Craton and need to be tested for kimberlites from other cratons.

5.5. Implications for diamond preservation

The studied xenoliths show complex petrographic signatures of metasomatism (Fig. 2), variable hydrogen distribution between the different nominally anhydrous minerals, and corresponding calculated water content (Table 3). A comparison of our estimates for the water concentration of peridotite xenoliths in Kaapvaal Craton kimberlites to those from the literature (Supplementary data-Table 1) highlights differences between the economic and uneconomic kimberlites. The lower water content recorded by xenoliths from kimberlites with low diamond content could be due to differences in the metasomatic history or water loss by hydrogen diffusion from olivine during kimberlite ascent. Certainly, if diamonds precipitate from reduced fluids in the lithosphere (Huizenga et al., 2012) then high-water activity during fluid metasomatism would be expected in the source of economic kimberlites. Alternatively, if diamond grade is governed by diamond preservation during kimberlite ascent, a slow ascent, known to be destructive for diamond would result on nominally anhydrous minerals losing more water and developing flat profiles, reflecting significant hydrogen diffusion. The dominance of flat olivine hydrogen

distribution profiles and rarity of the rare bell-shaped hydrogen loss profiles described in Hilchie et al. (2014), confirm hydrogen loss from the olivine to the surrounding melt and its re-equilibration. This could also imply a slower ascent of the kimberlite magma, allowing hydrogen to diffuse out, possibly re-equilibrate, and affecting diamond preservation.

The lower water concentration in olivine and orthopyroxene of the studied uneconomic xenoliths from the margin of the Kaapvaal craton in northern Lesotho as compared to the economic kimberlites equilibrated at similar pressures (Supplementary data-Table 1) further implies loss of water by the Lesotho kimberlites.

Additionally, studies of diamond surface features produced during pre-kimberlitic dissolution in the mantle source of diamonds have demonstrated that metasomatism destructive for diamonds is by melt and not fluid (Fedortchouk et al., 2019). However, metasomatism can exhibit dual behavior: if the metasomatic agent is CO_2-rich, it may lead to a decrease in water concentrations in nominally anhydrous minerals (NAMs), whereas a more water-dominated metasomatism can result in increased water concentrations in NAMs. Research on sheared peridotites from the mantle underneath Northern Lesotho by Heckel et al. (2023) indicates the lower lithosphere is affected by (proto-) kimberlitic melts, which metasomatized the mantle by traversing along the narrow shear zone networks produced by deformation at the lithosphere–asthenosphere boundary (LAB). The (proto-) kimberlitic/carbonate–silicate metasomatizing melt composition proposed by Heckel et al. (2023) is similar to the alkaline silico-carbonatite melt identified in this study and may be responsible for the metasomatism and diamond dissolution destruction in the mantle sampled by the uneconomic kimberlites.

The highly fragmented zones provide pathways for less viscous and low-density CO_2-rich fluids and carbonatitic melt. Moreover, deformation of the lithosphere along the craton margins, or in narrow shear zones at the contact between different lithospheric blocks (Irvine et al., 2001) may lead to higher permeability of these areas by the diffusion of hydrogen (Demouchy, 2010). The hydrogen liberated due to diffusion in shear zones may interact with the metasomatizing melt traversing in the shear zone networks and increase the water activity which is evidenced in high-water activity associated 3638 cm^{-1} band in the spectra of olivine in xenoliths from uneconomic kimberlites. The change in water activity is known to influence oxygen fugacity (Feig et al., 2010) and may affect the oxygen fugacity of the metasomatizing melt. Khokhryakov et al. (2021) demonstrate that high oxygen fugacity of H_2O-enriched melts of carbonate composition is most aggressive for diamond resorption at mantle temperatures. The 3638 cm^{-1} band identified in the discriminant analysis, and prominent in olivine spectra of peridotite xenoliths from uneconomic kimberlites (Fig. 4a, 4b and 4c), suggests stabilization at high water activity and oxygen fugacity. Thus, water enrichment of metasomatizing melt, driven by volatile diffusion in shear zones at the craton margin, may facilitate the diamond dissolution and could be responsible for the diamond loss in the uneconomic kimberlites.

The olivine water loss in xenoliths from uneconomic kimberlites, disruption of water between the different minerals by slow kimberlite ascent, allowing hydrogen to diffuse out and possibly re-equilibrate, provides a compelling evidence towards diamond destruction due to residence at shallower depths. However, the role of hydrogen diffusion in lithospheric shear zones at the margin of Kaapvaal craton, combined with evidenced melt metasomatism by alkaline silico-carbonatite melt in the uneconomic kimberlite xenoliths cannot be entirely ruled out. These factors may be

responsible for the diamond-poor nature of the uneconomic Northern Lesotho kimberlites, which are close to other economic ones from Northern Lesotho.

CRediT authorship contribution statement

Sahroz Khan: Conceptualization, Formal analysis, Investigation, Project administration, Visualization, Writing – original draft. **Nóra Liptai:** Data curation, Formal analysis, Methodology, Software, Writing – review & editing. **István J. Kovács:** Conceptualization, Funding acquisition, Methodology, Resources, Supervision, Writing – review & editing. **Yana Fedortchouk:** Conceptualization, Resources, Writing – review & editing, Supervision. **Tivadar M. Toth:** Conceptualization, Formal analysis, Funding acquisition, Methodology, Resources, Supervision, Writing – review & editing.

Declaration of competing interest

The authors declare that they have no known competing financial interests or personal relationships that could have appeared to influence the work reported in this paper.

Acknowledgments

Funding sources

Appendix A. Supplementary data

Supplementary data to this article can be found online at https://doi.org/10.1016/j.gr.2024.10.004.

References

Abersteiner, A., Golovin, A., Chayka, I., Kamenetsky, V.S., Goemann, K., Rodemann, T., Ehrig, K., 2022. Carbon compounds in the West Kimberley lamproites (Australia): Insights from melt and fluid inclusions. Gondwana Research 109, 536–557. https://doi.org/10.1016/j.gr.2022.06.005.

Aizawa, Y., Barnhoorn, A., Faul, U.H., Fitz Gerald, J.D., Jackson, I., Kovács, I., 2007. Seismic Properties of Anita Bay Dunite: an Exploratory Study of the Influence of Water. Journal of Petrology 49, 841–855. https://doi.org/10.1093/petrology/egn007.

Allsopp, H.L., Barrett, D.R., 1975. 40 - Rb–Sr age determinations on south African kimberlite pipes, in: Physics and Chemistry of the Earth. Elsevier, pp. 605–617. https://doi.org/10.1016/B978-0-08-018017-5.50044-4.

Aulbach, S., Giuliani, A., Fiorentini, M.L., Baumgartner, R.J., Savard, D., Kamenetsky, V.S., Caruso, S., Danyushevky, L.V., Powell, W., Griffin, W.L., 2021. Siderophile and chalcophile elements in spinels, sulphides and native Ni in strongly metasomatised xenoliths from the Bultfontein kimberlite (South Africa). Lithos 380–381, 105880. https://doi.org/10.1016/j.lithos.2020.105880.

Balan, E., Ingrin, J., Delattre, S., Kovács, I., Blanchard, M., 2011. Theoretical infrared spectrum of OH-defects in forsterite. European Journal of Mineralogy 23, 285–292. https://doi.org/10.1127/0935-1221/2011/0023-2090.

Baptiste, V., Tommasi, A., Demouchy, S., 2012. Deformation and hydration of the lithospheric mantle beneath the Kaapvaal craton, South Africa. Lithos 149, 31–50. https://doi.org/10.1016/j.lithos.2012.05.001.

Bell, D.R., Ihinger, P.D., Rossman, G.R., 1995. Quantitative analysis of trace OH in garnet and pyroxenes. American Mineralogist 80, 465–474. https://doi.org/10.2138/am-1995-5-607.

Bell, D.R., Grégoire, M., Grove, T.L., Chatterjee, N., Carlson, R.W., Buseck, P.R., 2005. Silica and volatile-element metasomatism of Archean mantle: a xenolith-scale example from the Kaapvaal Craton. Contributions to Mineralogy and Petrology 150, 251–267. https://doi.org/10.1007/s00410-005-0673-8.

Bell, D.R., Rossman, G.R., 1992. Water in Earth's Mantle: The Role of Nominally Anhydrous Minerals. Science 1979 (255), 1391–1397. https://doi.org/10.1126/science.255.5050.1391.

Bell, D.R., Rossman, G.R., Maldener, J., Endisch, D., Rauch, F., 2003. Hydroxide in olivine: A quantitative determination of the absolute amount and calibration of the IR spectrum. J Geophys Res Solid Earth 108. https://doi.org/10.1029/2001JB000679.

Bell, D.R., Rossman, G.R., Moore, R.O., 2004. Abundance and Partitioning of OH in a High-pressure Magmatic System: Megacrysts from the Monastery Kimberlite, South Africa. Journal of Petrology 45, 1539–1564. https://doi.org/10.1093/petrology/egh015.

Beran, A., Libowitzky, E., 2006. Water in Natural Mantle Minerals II: Olivine, Garnet and Accessory Minerals. Rev Mineral Geochem 62, 169–191. https://doi.org/10.2138/rmg.2006.62.8.

Berry, A.J., Hermann, J., O'Neill, H.S.C., Foran, G.J., 2005. Fingerprinting the water site in mantle olivine. Geology 33, 869. https://doi.org/10.1130/G21759.1.

Blanchard, M., Ingrin, J., Balan, E., Kovács, I., Withers, A.C., 2017. Effect of iron and trivalent cations on OH defects in olivine. American Mineralogist 102, 302–311. https://doi.org/10.2138/am-2017-5777.

Bonadiman, C., Hao, Y., Coltorti, M., Dallai, L., Faccini, B., Huang, Y.X., 2009. Water contents of pyroxenes in intraplate lithospheric mantle. European Journal of Mineralogy 21, 637–647. https://doi.org/10.1127/0935-1221/2009/0021-1935.

Boullier, A.M., Nicolas, A., 1975. Classification of textures and fabrics of peridotite xenoliths from South African kimberlites. Physics and Chemistry of the Earth 9, 467–475. https://doi.org/10.1016/0079-1946(75)90034-8.

Boyd, F.R., Nixon, P.H., 1975. Origins of the ultramafic nodules from some kimberlites of northern Lesotho and the Monastery Mine, South Africa. Physics and Chemistry of the Earth 9, 431–454. https://doi.org/10.1016/0079-1946(75)90032-4.

Bromiley, G.D., Keppler, H., McCammon, C., Bromiley, F.A., Jacobsen, S.D., 2004. Hydrogen solubility and speciation in natural, gem-quality chromian diopside. American Mineralogist 89, 941–949. https://doi.org/10.2138/am-2004-0703.

Brooker, R.A., Sparks, R.S.J., Kavanagh, J.L., Field, M., 2011. The volatile content of hypabyssal kimberlite magmas: some constraints from experiments on natural rock compositions. Bull Volcanol 73, 959–981. https://doi.org/10.1007/s00445-011-0523-7.

Chukanov, N. V., Chervonnyi, A.D., 2016. Some General Aspects of the Application of IR Spectroscopy to the Investigation of Minerals. pp. 1–49. https://doi.org/10.1007/978-3-319-25349-7_1.

Clement, C.R., 1982. A comparative geological study of some major kimberlite pipes in the Northern Cape and Orange Free State (PhD). University of Cape Town, Cape Town.

Cox, K.G., Gurney, J., Harte, B., 1973. Xenoliths from the Matsoku Pipe, in: Nixon, P. H. (Ed.), Lesotho Kimberlites. Lesotho National Development Corporation, pp. 76–91.

Davis, G.L., 1977. The ages and uranium contents of zircons from kimberlites and associated rocks. International Kimberlite Conference Extended Abstracts. University of Alberta.

de Wit, M., Bhebhe, Z., Davidson, J., Haggerty, S.E., Hundt, P., Jacob, J., Lynn, M., Marshall, T.R., Skinner, C., Smithson, K., Stiefenhofer, J., Robert, M., Revitt, A., Spaggiari, R.S., Ward, J., 2016. Overview of Diamond Resources in Africa. Episodes 39, 199–237 https://doi.org/10.18814/epiiugs/2016/v39i2/95776.

de Wit, M.J., de Ronde, C.E.J., Tredoux, M., Roering, C., Hart, R.J., Armstrong, R.A., Green, R.W.E., Peberdy, E., Hart, R.A., 1992. Formation of an Archaean continent. Nature 357, 553–562. https://doi.org/10.1038/357553a0.

Della Ventura, G., Oberti, R., Hawthorne, F.C., Bellatreccia, F., 2007. FTIR spectroscopy of Ti-rich pargasites from Lherz and the detection of O2 at the anionic O3 site in amphiboles. American Mineralogist 92, 1645–1651. https://doi.org/10.2138/am.2007.2199.

Demouchy, S., 2010. Diffusion of hydrogen in olivine grain boundaries and implications for the survival of water-rich zones in the Earth's mantle. Earth Planet Sci Lett 295, 305–313. https://doi.org/10.1016/j.epsl.2010.04.019.

Demouchy, S., Bolfan-Casanova, N., 2016. Distribution and transport of hydrogen in the lithospheric mantle: A review. Lithos 240–243, 402–425. https://doi.org/10.1016/j.lithos.2015.11.012.

Doucet, L.S., Peslier, A.H., Ionov, D.A., Brandon, A.D., Golovin, A.V., Goncharov, A.G., Ashchepkov, I.V., 2014. High water contents in the Siberian cratonic mantle linked to metasomatism: An FTIR study of Udachnaya peridotite xenoliths. Geochim Cosmochim Acta 137, 159–187. https://doi.org/10.1016/j.gca.2014.04.011.

Fabbrizio, A., Stalder, R., Hametner, K., Günther, D., Marquardt, K., 2013. Experimental partitioning of halogens and other trace elements between olivine, pyroxenes, amphibole and aqueous fluid at 2 GPa and 900–1,300 °C. Contributions to Mineralogy and Petrology 166, 639–653. https://doi.org/10.1007/s00410-013-0902-5.

Fedortchouk, Y., Canil, D., Semenets, E., 2007. Mechanisms of diamond oxidation and their bearing on the fluid composition in kimberlite magmas. American Mineralogist 92, 1200–1212. https://doi.org/10.2138/am.2007.2416.

Fedortchouk, Y., Liebske, C., McCammon, C., 2019. Diamond destruction and growth during mantle metasomatism: An experimental study of diamond resorption features. Earth Planet Sci Lett 506, 493–506. https://doi.org/10.1016/j.epsl.2018.11.025.

Fedortchouk, Y., Chinn, I.L., Perritt, S.H., Zhang, Z., Stern, R.A., Li, Z., 2022. Diamond-destructive mantle metasomatism: Evidence from the internal and external textures of diamonds and their nitrogen defects. Lithos 414–415, 106616. https://doi.org/10.1016/j.lithos.2022.106616.

Feig, S.T., Koepke, J., Snow, J.E., 2010. Effect of oxygen fugacity and water on phase equilibria of a hydrous tholeiitic basalt. Contributions to Mineralogy and Petrology 160, 551–568. https://doi.org/10.1007/s00410-010-0493-3.

Field, M., Stiefenhofer, J., Robey, J., Kurszlaukis, S., 2008. Kimberlite-hosted diamond deposits of southern Africa: A review. Ore Geol Rev 34, 33–75. https://doi.org/10.1016/j.oregeorev.2007.11.002.

Fullea, J., 2017. On Joint Modelling of Electrical Conductivity and Other Geophysical and Petrological Observables to Infer the Structure of the Lithosphere and Underlying Upper Mantle. Surv Geophys 38, 963–1004. https://doi.org/10.1007/s10712-017-9432-4.

Giuliani, A., Pearson, D.G., Soltys, A., Dalton, H., Phillips, D., Foley, S.F., Lim, E., Goemann, K., Griffin, W.L., Mitchell, R.H., 2020. Kimberlite genesis from a common carbonate-rich primary melt modified by lithospheric mantle assimilation. Science Advances 6 (17), p.eaaz0424.

Golovin, A.V., Sharygin, V.V., Pokhilenko, N.P., 2007. Melt inclusions in olivine phenocrysts in unaltered kimberlites from the Udachnaya-East pipe, Yakutia: Some aspects of kimberlite magma evolution during late crystallization stages. Petrology 15, 168–183. https://doi.org/10.1134/S086959110702004X.

Golovin, A.V., Sharygin, I.S., Korsakov, A.V., Kamenetsky, V.S., Abersteiner, A., 2020. Can primitive kimberlite melts be alkali-carbonate liquids: Composition of the melt snapshots preserved in deepest mantle xenoliths: Journal of Raman Spectroscopy 51, 1849–1867. https://doi.org/10.1002/jrs.5701.

Grant, K., Ingrin, J., Lorand, J.P., Dumas, P., 2007. Water partitioning between mantle minerals from peridotite xenoliths. Contributions to Mineralogy and Petrology 154, 15–34. https://doi.org/10.1007/s00410-006-0177-1.

Green, D.H., Hibberson, W.O., Kovács, I., Rosenthal, A., 2010. Water and its influence on the lithosphere–asthenosphere boundary. Nature 467, 448–451. https://doi.org/10.1038/nature09369.

Gregoire, M., Bell, D.R., LE Roex, A.P., 2003. Garnet Lherzolites from the Kaapvaal Craton (South Africa): Trace Element Evidence for a Metasomatic History. Journal of Petrology 44, 629–657. https://doi.org/10.1093/petrology/44.4.629.

Griffin, W.L., O'Reilly, S.Y., 2007. Chapter 8.2 The Earliest Subcontinental Lithospheric Mantle. pp. 1013–1035. https://doi.org/10.1016/S0166-2635(07)15082-9.

Griffin, W., O'Reilly, S.Y., Natapov, L.M., Ryan, C.G., 2003. The evolution of lithospheric mantle beneath the Kalahari Craton and its margins. Lithos 71, 215–241. https://doi.org/10.1016/j.lithos.2003.07.006.

Grove, T., Chatterjee, N., Parman, S., Medard, E., 2006. The influence of H2O on mantle wedge melting. Earth Planet Sci Lett 249, 74–89. https://doi.org/10.1016/j.epsl.2006.06.043.

Harte, B., 1983. Mantle peridotites and process–the kimberlite sample. In: Hawkesworthy, C.J., Norry, M.J. (Eds.), Continental Basalts and Their Mantle Xenoliths. Shiva Publishing Limited, Nantwitch, Cheshire, pp. 46–91.

Harte, B., Winterburn, P.A., Gurney, J.J., 1987. Metasomatic and enrichment phenomena in garnet peridotite facies mantle xenoliths from the Matsoku Kimberlite Pipe (Lesotho). In: Menzies, M.A., Hawkesworth, C.J. (Eds.), Mantle Metasomatism, Academic Press. Academic Press, London, pp. 145–220.

Harte, B., Hunter, R.H., Kinny, P.D., 1993. Melt geometry, movement and crystallization, in relation to mantle dykes, veins and metasomatism. Philosophical Transactions of the Royal Society of London. Series a: Physical and Engineering Sciences 342, 1–21. https://doi.org/10.1098/rsta.1993.0001.

Heckel, C., Woodland, A.B., Linckens, J., Gibson, S.A., Seitz, H.-M., 2023. Sheared Peridotites from Northern Lesotho: Metasomatism-Induced Deformation and Craton Destabilization. Journal of Petrology 64. https://doi.org/10.1093/petrology/egad076.

Hilchie, L., 2011. Zonation of hydrogen in kimberlitic and mantle olivines: a possible proxy for the water content of kimberlite magmas. Dalhousie University, Halifax.

Hilchie, L., Fedortchouk, Y., Matveev, S., Kopylova, M.G., 2014. The origin of high hydrogen content in kimberlitic olivine: Evidence from hydroxyl zonation in olivine from kimberlites and mantle xenoliths. Lithos 202–203, 429–441. https://doi.org/10.1016/j.lithos.2014.06.010.

Huizenga, J.M., Crossingham, A., Viljoen, F., 2012. Diamond precipitation from ascending reduced fluids in the Kaapvaal lithosphere: thermodynamic constraints. Comptes Rendus Geoscience 344 (2), 67–76.

Ingrin, J., Grégoire, M., 2010. Water partitioning in spinel and garnet lherzolites xenoliths from the same kimberlite pipe (Premier Mine, Kaapvaal, South Africa). In: EGU General Assembly Conference Abstracts.

Ingrin, J., Kovács, I., Deloule, E., Balan, E., Blanchard, M., Kohn, S.C., Hermann, J., 2014. Identification of hydrogen defects linked to boron substitution in synthetic forsterite and natural olivine. American Mineralogist 99, 2138–2141. https://doi.org/10.2138/am-2014-5049.

Irvine, G.J., Pearson, D.G., Carlson, R.W., 2001. Lithospheric mantle evolution of the Kaapvaal Craton: A Re-Os isotope study of peridotite xenoliths from Lesotho kimberlites. Geophys Res Lett 28, 2505–2508. https://doi.org/10.1029/2000GL012411.

Jackson, C.G., Gibson, S.A., 2023. Build-up of multiple volatiles in Earth's continental keels: Implications for craton stability. Earth Planet Sci Lett 611, 118134. https://doi.org/10.1016/j.epsl.2023.118134.

Jacobs, J., Pisarevsky, S., Thomas, R.J., Becker, T., 2008. The Kalahari Craton during the assembly and dispersal of Rodinia. Precambrian Res 160, 142–158. https://doi.org/10.1016/j.precamres.2007.04.022.

Jollands, M.C., Hanger, B.J., Yaxley, G.M., Hermann, J., Kilburn, M.R., 2018. Timescales between mantle metasomatism and kimberlite ascent indicated by diffusion profiles in garnet crystals from peridotite xenoliths. Earth Planet Sci Lett 481, 143–153. https://doi.org/10.1016/j.epsl.2017.10.021.

Katz, R.F., Spiegelman, M., Langmuir, C.H., 2003. A new parameterization of hydrous mantle melting. Geochemistry, Geophysics, Geosystems 4. https://doi.org/10.1029/2002GC000433.

Kent, A.J.R., Rossman, G.R., 2002. Hydrogen, lithium, and boron in mantle-derived olivine: The role of coupled substitutions. American Mineralogist 87, 1432–1436. https://doi.org/10.2138/am-2002-1020.

Khokhryakov, A.F., Kruk, A.N., Sokol, A.G., 2021. The effect of oxygen fugacity on diamond resorption in ascending kimberlite melt. Lithos 394–395, 106166. https://doi.org/10.1016/j.lithos.2021.106166.

Khokhryakov, A.F., Pal'yanov, Y.N., 2010. Influence of the fluid composition on diamond dissolution forms in carbonate melts. American Mineralogist 95 (10), 1508–1514.

Kobussen, A.F., Griffin, W.L., O'Reilly, S.Y., Shee, S.R., 2008. Ghosts of lithospheres past: Imaging an evolving lithospheric mantle in southern Africa. Geology 36, 515. https://doi.org/10.1130/G24868A.1.

Kobussen, A.F., Griffin, W.L., O'Reilly, S.Y., 2009. Cretaceous thermo-chemical modification of the Kaapvaal cratonic lithosphere, South Africa. Lithos 112, 886–895. https://doi.org/10.1016/j.lithos.2009.06.031.

Koch-Müller, M., Matsyuk, S.S., Wirth, R., 2004. Hydroxyl in omphacites and omphacitic clinopyroxenes of upper mantle to lower crustal origin beneath the Siberian platform. American Mineralogist 89, 921–931. https://doi.org/10.2138/am-2004-0701.

Koch-Müller, M., Matsyuk, S.S., Rhede, D., Wirth, R., Khisina, N., 2006. Hydroxyl in mantle olivine xenocrysts from the Udachnaya kimberlite pipe. Phys Chem Miner 33, 276–287. https://doi.org/10.1007/s00269-006-0079-9.

Kostrovitsky, S., Dymshits, A., Yakovlev, D., Sun, J., Kalashnikova, T., Ashchepkov, I., Belozerova, O., 2023. Primary Composition of Kimberlite Melt. Minerals 13 (11), 1404.

Kovács, I., Hermann, J., O'Neill, H., St, C., Gerald, J.F., Sambridge, M., Horvath, G., 2008. Quantitative absorbance spectroscopy with unpolarized light: Part II. Experimental evaluation and development of a protocol for quantitative analysis of mineral IR spectra. American Mineralogist 93, 765–778. https://doi.org/10.2138/am.2008.2656.

Kovács, I., O'Neill, H., St, C., Hermann, J., Hauri, E.H., 2010. Site-specific infrared O-H absorption coefficients for water substitution into olivine. American Mineralogist 95, 292–299. https://doi.org/10.2138/am.2010.3313.

Kovács, I., Green, D.H., Rosenthal, A., Hermann, J., O'neill, H.St.C., Hibberson, W.O., Udvardi, A., 2012. An Experimental Study of Water in Nominally Anhydrous Minerals in the Upper Mantle near the Water-saturated Solidus. Journal of Petrology 53, 2067–2093. https://doi.org/10.1093/petrology/egs044.

Kovács, I., Demény, A., Czuppon, G., Lécuyer, C., Fourel, F., Xia, Q.-K., Liu, J., Pintér, Z., Király, E., Török, K., Szabó, Á., Deloule, E., Falus, G., Fancsik, T., Zajacz, Z., Sándorné Kovács, J., Udvardi, B., 2016. Water concentrations and hydrogen isotope compositions of alkaline basalt-hosted clinopyroxene megacrysts and amphibole clinopyroxenites: the role of structural hydroxyl groups and molecular water. Contributions to Mineralogy and Petrology 171, 38. https://doi.org/10.1007/s00410-016-1241-0.

Kresten, P., Dempster, A.N., 1973. The Geology of Pipe 200 and the Malibamatso Dyke Swarm. Lesotho National Development Corporation.

Kurosawa, M., Yurimoto, H., Sueno, S., 1997. Patterns in the hydrogen and trace element compositions of mantle olivines. Phys Chem Miner 24, 385–395. https://doi.org/10.1007/s002690050052.

Lawless, P.J., Gurney, J.J., Dawson, J.B., 1979. Polymict peridotites from the Bultfontein And De Beers mines, Kimberly, South Africa, in: The Mantle Sample: Inclusion in Kimberlites and Other Volcanics. American Geophysical Union, Washington, D. C., pp. 145–155. https://doi.org/10.1029/SP016p0145.

Lazarov, M., Brey, G.P., Weyer, S., 2012. Evolution of the South African mantle — A case study of garnet peridotites from the Finsch diamond mine (Kaapvaal craton); part 1: Inter-mineral trace element and isotopic equilibrium. Lithos 154, 193–209. https://doi.org/10.1016/j.lithos.2012.07.007.

Liptai, N., Lange, T.P., Patkó, L., Pintér, Z., Berkesi, M., Aradi, L.E., Szabó, C., Kovács, I.J., 2021. Effect of water on the rheology of the lithospheric mantle in young extensional basin systems as shown by xenoliths from the Carpathian-Pannonian region. Glob Planet Change 196, 103364. https://doi.org/10.1016/j.gloplacha.2020.103364.

Liptai, N., Lange, T.P., Patkó, L., László, E.A., Berkesi, M., Peter, M.E.T., José, A.-P.-N., Jörg, H., Gergely, S., Szabó, C., Kovács, I.J., 2023. Formation of amphibole lamellae in mantle pyroxene by fluid-mediated metasomatism: A focal plane array FTIR study from the Carpathian-Pannonian region. American Mineralogist. https://doi.org/10.2138/am-2022-8662.

Madejová, J., Gates, W.P., Petit, S., 2017. IR Spectra of Clay Minerals. pp. 107–149. https://doi.org/10.1016/B978-0-08-100355-8.00005-9.

Matsyuk, S.S., Langer, K., 2004. Hydroxyl in olivines from mantle xenoliths in kimberlites of the Siberian platform. Contributions to Mineralogy and Petrology 147, 413–437. https://doi.org/10.1007/s00410-003-0541-3.

Mierdel, K., Keppler, H., Smyth, J.R., Langenhorst, F., 2007. Water Solubility in Aluminous Orthopyroxene and the Origin of Earth's Asthenosphere. Science 1979 (315), 364–368. https://doi.org/10.1126/science.1135422.

Miller, G.H., Rossman, G.R., Harlow, G.E., 1987. The natural occurrence of hydroxide in olivine. Phys Chem Miner 14, 461–472. https://doi.org/10.1007/BF00628824.

Mitchell, R.H., Carswell, D.A., Clarke, D.B., 1980. Geological implications and validity of calculated equilibration conditions for ultramafic xenoliths from the pipe 200 kimberlite, northern Lesotho. Contributions to Mineralogy and Petrology 72, 205–217. https://doi.org/10.1007/BF00399481.

Mosenfelder, J.L., Le Voyer, M., Rossman, G.R., Guan, Y., Bell, D.R., Asimow, P.D., Eiler, J.M., 2011. Analysis of hydrogen in olivine by SIMS: Evaluation of standards and protocol. American Mineralogist 96, 1725–1741. https://doi.org/10.2138/am.2011.3810.

Moussallam, Y., Morizet, Y., Massuyeau, M., Laumonier, M., Gaillard, F., 2015. CO_2 solubility in kimberlite melts. Chem Geol 418, 198–205. https://doi.org/10.1016/j.chemgeo.2014.11.017.

Novella, D., Bolfan-Casanova, N., Nestola, F., Harris, J.W., 2015. H_2O in olivine and garnet inclusions still trapped in diamonds from the Siberian craton: Implications for the water content of cratonic lithosphere peridotites. Lithos 230, 180–183. https://doi.org/10.1016/j.lithos.2015.05.013.

O'Leary, J.A., Gaetani, G.A., Hauri, E.H., 2010. The effect of tetrahedral Al^{3+} on the partitioning of water between clinopyroxene and silicate melt. Earth Planet Sci Lett 297, 111–120. https://doi.org/10.1016/j.epsl.2010.06.011.

O'Reilly, S.Y., Griffin, W.L., 2010. The continental lithosphere–asthenosphere boundary: Can we sample it? Lithos 120, 1–13. https://doi.org/10.1016/j.lithos.2010.03.016.

Olive, V., Ellam, R.M., Harte, B., 1997. A Re—Os isotope study of ultramafic xenoliths from the Matsoku kimberlite. Earth Planet Sci Lett 150, 129–140. https://doi.org/10.1016/S0012-821X(97)00088-5.

Palyanov, Y.N., Sokol, A.G., 2009. The effect of composition of mantle fluids/melts on diamond formation processes. Lithos 112, 690–700.

Patkó, L., Liptai, N., Kovács, I.J., Aradi, L.E., Xia, Q.-K., Ingrin, J., Mihály, J., O'Reilly, S.Y., Griffin, W.L., Wesztergom, V., Szabó, C., 2019. Extremely low structural hydroxyl contents in upper mantle xenoliths from the Nógrád-Gömör Volcanic Field (northern Pannonian Basin): Geodynamic implications and the role of post-eruptive re-equilibration. Chem Geol 507, 23–41. https://doi.org/10.1016/j.chemgeo.2018.12.017.

Pearson, D.G., Canil, D., Shirey, S.B., 2003. Mantle Samples Included in Volcanic Rocks: Xenoliths and Diamonds, in: Treatise on Geochemistry. Elsevier, pp. 171–275. https://doi.org/10.1016/B0-08-043751-6/02005-3.

Pearson, D.G., Woodhead, J., Janney, P.E., 2019. Kimberlites as geochemical probes of Earth's mantle. Elements: an International Magazine of Mineralogy, Geochemistry, and Petrology 15 (6), 387–392.

Peslier, A.H., 2010. A review of water contents of nominally anhydrous natural minerals in the mantles of Earth, Mars and the Moon. Journal of Volcanology and Geothermal Research 197, 239–258. https://doi.org/10.1016/j.jvolgeores.2009.10.006.

Peslier, A., Luhr, J., 2006. Hydrogen loss from olivines in mantle xenoliths from Simcoe (USA) and Mexico: Mafic alkalic magma ascent rates and water budget of the sub-continental lithosphere. Earth Planet Sci Lett 242, 302–319. https://doi.org/10.1016/j.epsl.2005.12.019.

Peslier, A.H., Woodland, A.B., Wolff, J.A., 2008. Fast kimberlite ascent rates estimated from hydrogen diffusion profiles in xenolithic mantle olivines from southern Africa. Geochim Cosmochim Acta 72, 2711–2722. https://doi.org/10.1016/j.gca.2008.03.019.

Peslier, A.H., Woodland, A.B., Bell, D.R., Lazarov, M., 2010. Olivine water contents in the continental lithosphere and the longevity of cratons. Nature 467, 78–81. https://doi.org/10.1038/nature09317.

Peslier, A.H., Woodland, A.B., Bell, D.R., Lazarov, M., Lapen, T.J., 2012. Metasomatic control of water contents in the Kaapvaal cratonic mantle. Geochim Cosmochim Acta 97, 213–246. https://doi.org/10.1016/j.gca.2012.08.028.

Prechtel, F., Stalder, R., 2011. The potential use of OH-defects in enstatite as geobarometer. Contributions to Mineralogy and Petrology 162, 615–623. https://doi.org/10.1007/s00410-011-0615-6.

Prechtel, F., Stalder, R., 2012. OH-defects in Al- and Cr- doped synthetic enstatites and defect geobarometry on natural orthopyroxenes from the Earth's mantle. European Journal of Mineralogy 24, 471–481. https://doi.org/10.1127/0935-1221/2012/0024-2208.

Richardson, S.H., Erlank, A.J., Harris, J.W., Hart, S.R., 1990. Eclogitic diamonds of Proterozoic age from Cretaceous kimberlites. Nature 346, 54–56. https://doi.org/10.1038/346054a0.

Richardson, S.H., Shirey, S.B., Harris, J.W., Carlson, R.W., 2001. Archean subduction recorded by Re–Os isotopes in eclogitic sulfide inclusions in Kimberley diamonds. Earth Planet Sci Lett 191, 257–266. https://doi.org/10.1016/S0012-821X(01)00419-8.

Riley, T.R., Leat, P.T., Curtis, M.L., 2006. Karoo large igneous province: Brevity, origin, and relation to mass extinction questioned by new 40Ar/39Ar age data: Comment: COMMENT. Geology 34, e109–e110. https://doi.org/10.1130/G22380C.1.

Sambridge, M., Gerald, J.F., Kovács, I., O'Neill, H., St, C., Hermann, J., 2008. Quantitative absorbance spectroscopy with unpolarized light: Part I. Physical and Mathematical Development. American Mineralogist 93, 751–764. https://doi.org/10.2138/am.2008.2657.

Schmitz, M.D., Bowring, S.A., de Wit, M.J., Gartz, V., 2004. Subduction and terrane collision stabilize the western Kaapvaal craton tectosphere 2.9 billion years ago. Earth Planet Sci Lett 222, 363–376. https://doi.org/10.1016/j.epsl.2004.03.036.

Scoates, J.S., Friedman, R.M., 2008. Precise age of the platiniferous Merensky Reef, Bushveld Complex, South Africa, by the U-Pb zircon chemical abrasion ID-TIMS technique. Economic Geology 103, 465–471. https://doi.org/10.2113/gsecongeo.103.3.465.

Sharygin, I.S., Golovin, A.V., Tarasov, A.A., Dymshits, A.M., Kovaleva, E., 2022. Confocal Raman spectroscopic study of melt inclusions in olivine of mantle xenoliths from the Bultfontein kimberlite pipe (Kimberley cluster, South Africa): Evidence for alkali-rich carbonate melt in the mantle beneath Kaapvaal Craton. Journal of Raman Spectroscopy 53, 508–524. https://doi.org/10.1002/jrs.6198.

Simon, N.S.C., Carlson, R.W., Pearson, D.G., Davies, G.R., 2007. The Origin and Evolution of the Kaapvaal Cratonic Lithospheric Mantle. Journal of Petrology 48, 589–625. https://doi.org/10.1093/petrology/egl074.

Skyes, D., Rossman, G.R., Veblen, D.R., Grew, E.S., 1997. Enhanced H and F incorporation in borian olivine. American Mineralogist 79, 904–908.

Smith, E.M., Kopylova, M.G., Frezzotti, M.L., Afanasiev, V.P., 2015. Fluid inclusions in Ebelyakh diamonds: Evidence of CO_2 liberation in eclogite and the effect of H_2O on diamond habit. Lithos 216–217, 106–117. https://doi.org/10.1016/j.lithos.2014.12.010.

Sokol, A.G., Kupriyanov, I.N., Palyanov, Y.N., 2013. Partitioning of H_2O between olivine and carbonate–silicate melts at 6.3 GPa and 1400 C: Implications for kimberlite formation. Earth and Planetary Science Letters 383, 58–67.

Stalder, R., Ludwig, T., 2007. OH incorporation in synthetic diopside. European Journal of Mineralogy 19, 373–380. https://doi.org/10.1127/0935-1221/2007/0019-1721.

Stalder, R., Skogby, H., 2003. Hydrogen diffusion in natural and synthetic orthopyroxene. Phys Chem Miner 30, 12–19. https://doi.org/10.1007/s00269-002-0285-z.

Stalder, R., Skogby, H., 2007. Dehydration mechanisms in synthetic Fe-bearing enstatite. European Journal of Mineralogy 19, 201–216. https://doi.org/10.1127/0935-1221/2007/0019-1710.

Tappe, S., Smart, K., Torsvik, T., Massuyeau, M., de Wit, M., 2018. Geodynamics of kimberlites on a cooling Earth: Clues to plate tectonic evolution and deep volatile cycles. Earth and Planetary Science Letters 484, 1–14.

Tappe, S., Massuyeau, M., Smart, K.A., Woodland, A.B., Gussone, N., Milne, S., Stracke, A., 2021. Sheared Peridotite and Megacryst Formation Beneath the Kaapvaal Craton: a Snapshot of Tectonomagmatic Processes across the Lithosphere-Asthenosphere Transition. Journal of Petrology 62. https://doi.org/10.1093/petrology/egab046.

Tollan, P.M.E., Smith, R., O'Neill, H., St, C., Hermann, J., 2017. The responses of the four main substitution mechanisms of H in olivine to H_2O activity at 1050 °C and 3 GPa. Prog Earth Planet Sci 4, 14. https://doi.org/10.1186/s40645-017-0128-7.

Toth, V., Schulze, D.J., 2017. Mg-metasomatized Fe-rich dunites from the Thaba Putsoa kimberlite, Lesotho: headstones in a kimberlite graveyard. International Kimberlite Conference Extended Abstracts. University of Alberta.

Wasch, L.J., van der Zwan, F.M., Nebel, O., Morel, M.L.A., Hellebrand, E.W.G., Pearson, D.G., Davies, G.R., 2009. An alternative model for silica enrichment in the Kaapvaal subcontinental lithospheric mantle. Geochim Cosmochim Acta 73, 6894–6917. https://doi.org/10.1016/j.gca.2009.07.038.

Weiss, Y., Kiro, Y., Class, C., Winckler, G., Harris, J.W., Goldstein, S.L., 2021. Helium in diamonds unravels over a billion years of craton metasomatism. Nat Commun 12, 2667. https://doi.org/10.1038/s41467-021-22860-3.

Withers, A.C., Hirschmann, M.M., Tenner, T.J., 2011. The effect of Fe on olivine H_2O storage capacity: Consequences for H_2O in the martian mantle. American Mineralogist 96, 1039–1053. https://doi.org/10.2138/am.2011.3669.

Yang, X., 2016. Effect of oxygen fugacity on OH dissolution in olivine under peridotite-saturated conditions: An experimental study at 1.5–7 GPa and 1100–1300 °C. Geochim Cosmochim Acta 173, 319–336. https://doi.org/10.1016/j.gca.2015.11.007.

Yang, X., Ingrin, J., Liu, W., Huang, W., Gu, X., Xia, Q., 2021. Behavior and origin of hydrogen defects in natural orthopyroxene during high-temperature processes. American Mineralogist 106, 1768–1779. https://doi.org/10.2138/am-2021-7741.